

Techniques for Particle Identification

Tom Ypsilantis
Collège de France
Lab. de Physique Corpusculaire
11 Place Marcelin-Berthelot
F-75231
Paris CEDEX 05
FRANCE

Lecture One: Introduction

Material not available. Please refer to the Summer Institute Prelecture Notes.

Lecture Two: A Long Baseline RICH with a 27-Kiloton Water Target and Radiator for Detection of Neutrino Oscillations

T. Ypsilantis,^{(a)*} J. Séguinot,^(a) and A. Zichichi^(b)

(a) Collège de France

(b) Università di Bologna

*Lecturer, tel: (004122) 767 7577, fax: (004122) 785 0207, e-mail: thomas.ypsilantis@cern.ch.

©1995 by Tom Ypsilantis.

LECTURE TWO:

A Long Baseline RICH with a 27-Kiloton Water Target and Radiator for Detection of Neutrino Oscillations

T. Ypsilantis,^{(a)*} J. Séguinot,^(a) and A. Zichichi^(b)

(a) College de France

(b) Università di Bologna

ABSTRACT

A 27 kt water volume is investigated as a target for a long baseline neutrino beam from CERN to Gran Sasso. Charged secondaries from the neutrino interactions produce Cherenkov photons in water which are imaged as rings by a spherical mirror.

The photon detector elements are 14 400 photomultipliers (PM's) of 127 mm diameter or 3600 HPD's of 250 mm diameter with single photon sensitivity. A coincidence signal of about 300 pixel elements in time with the SPS beam burst starts readout in bins of 1 ns over a period of 128 ns.

Momentum, direction, and velocity of hadrons and muons are determined from the width, center, and radius of the rings, respectively. Momentum is measured if multiple scattering dominates the ring width, as is the case for most of the particles of interest.

Momentum resolutions of 1-10%, mass resolutions of 5-50 MeV, and direction resolutions of < 1 mrad are achievable. Thresholds in water for muons, pions, kaons, and protons are 0.12, 0.16, 0.55, and 1.05 GeV/c, respectively.

Electrons and gammas can be measured with energy resolution $\sigma_E/E = 8.5\%/\sqrt{E(\text{GeV})}$ and with direction resolution ≈ 1 mrad.

The detector can be sited either inside a Gran Sasso tunnel or above ground because it is directional and the SPS beam is pulsed; thus the rejection of cosmic ray background is excellent.

1. Introduction

The lectures covered our recent work on TEA-Fast RICH counters [1], on CsI-Fast RICH counters [2], and new results on HPD photodetectors for RICH [3]. Since these works are now published, we refer the interested reader to the above references and concentrate here on the final seminar on long baseline RICH (LBL-RICH) [4].

1.1 Long Baseline RICH

The question of neutrino masses and mixing remains one of the most important unsolved problems of particle physics. Experiments in this field use either accelerator neutrinos, solar neutrinos, or atmospheric neutrinos, each sensitive to a different range of neutrino masses and mixing angles. Italy and CERN are now considering a neutrino beam traversing 732 km of earth to arrive at the Laboratorio Nazionale Gran Sasso (LNGS), where long baseline experiments will be installed. The possibility for such experiments was already among the physics goals of the Gran Sasso Project and special care was taken to build the experimental halls aligned towards CERN [5]. The advantage of long baseline neutrino experiments is, of course, their increased sensitivity to small mass differences.

For this purpose, the large water radiator and RICH detector, shown schematically in Fig. 1, was proposed as an experiment at the Gran Sasso laboratory [6]. The water is cheap and safe, and serves both

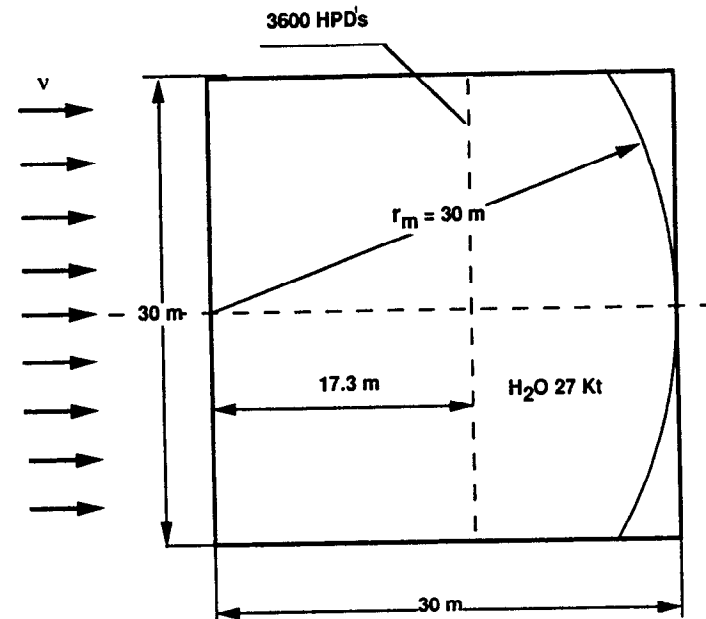


Fig. 1. The layout of the 27 kt water target and radiator between $z = 0$ to $z = 30$ m with $x = \pm 15$ m, and $y = \pm 15$ m. A mirror of curvature $r_m = 30$ m is at position $z = 30$ m.

as the neutrino target and the radiating medium. Cherenkov photons, produced by charged particles from neutrino interactions in the water, are detected with visible light photomultipliers (PM's). All hardware elements of this experiment (i.e., clean water, PM's, mirrors, and a swimming pool of Olympic volume) are completely proven and do not require additional R&D.

Of course, most of these elements were (are) present in the pioneering IMB, Kamiokande (and the new 50 kt Super-Kamiokande) detectors which investigate(d) solar neutrinos, atmospheric neutrino interactions, and proton decay.

Our technique, however, differs in one essential aspect, namely, its use of a mirror to give focused images which allow momentum, velocity, and mass determination from Cherenkov rings which are multiple scattering dominated (MSD). Without the mirror, the ring width is determined by track length, which itself is of little direct physical interest but prohibits the observation of multiple scattering which can determine momentum.

1.2 Some Basic Cherenkov Relations

The Cherenkov emission angle θ relative to the particle direction is given by Cherenkov's equation

$$\cos\theta = \frac{1}{n\beta}, \quad (1)$$

where n is the radiator refractive index and β the particle velocity. The number of detected photoelectrons N is given by the integral of the Frank-Tamm relation

$$N = N_0 Z^2 L \sin^2 \theta, \quad (2)$$

where L is the particle pathlength in the medium, Ze the particle charge, and N_0 is the detector response parameter defined as

$$N_0 = (\alpha / \hbar c) \int (QTR) dE = (370 \text{ eV}^{-1} \text{ cm}^{-1}) TR q_{\text{int}}, \quad (3)$$

and α is the fine structure constant, E the photon energy, $q_{\text{int}} = \int Q dE$ the energy integral of quantum efficiency, T the radiator transmission, and R the mirror reflectivity. A glass window, visible light PM has Q varying from 4 to 28% for E from 2 to 3.5 eV. Integration gives $q_{\text{int}} = 0.32 \text{ eV}$ and for $R = 0.95$ and $T = 1$, we find $N_0 = 112/\text{cm}$ for full PM coverage and $N_0 = 22/\text{cm}$ for 20% coverage. Thus, in water, we expect one detected photoelectron per mm of pathlength [from Eq. (2) for $n = 1.34$, $Z = \beta = 1$, $\sin^2 \theta \approx 0.44$, thus $N/L \approx 1/\text{mm}$].

1.3 Momentum from RICH

It is well-known that a ring image determines particle direction (i.e., the polar and azimuthal angles θ_p, ϕ_p) from the ring center and

particle velocity β from the ring radius [7]. Using $p = m\beta\gamma$ as the defining relation for momentum, we obtain the error

$$\frac{\sigma_p}{p} = \sqrt{\left(\frac{\sigma_m}{m}\right)^2 + \left(\gamma^2 \frac{\sigma_\beta}{\beta}\right)^2}, \quad (4)$$

where m is assumed to be measured with error σ_m . The velocity resolution obtainable from RICH is $\sigma_\beta/\beta = \tan\theta\sigma_\theta/\sqrt{N}$ with θ the image radius and σ_θ the image width (per photon) [7], thus

$$\frac{\sigma_p}{p} = \sqrt{\left(\frac{\sigma_m}{m}\right)^2 + \left(\gamma^2 \frac{\tan\theta\sigma_\theta}{\sqrt{N}}\right)^2}. \quad (5)$$

Obviously, m must be measured in order to determine p ; moreover, Eq. (5) shows that the error from β (the second term) degrades as γ^2 thus is rapidly limited at high momenta. Neither p or σ_p/p can be found without m ; however, to measure m , we must use the same defining relation $m = p/\beta\gamma$ and by the same argument obtain Eq. (5) in a different form, i.e.,

$$\frac{\sigma_m}{m} = \sqrt{\left(\frac{\sigma_p}{p}\right)^2 + \left(\gamma^2 \frac{\tan\theta\sigma_\theta}{\sqrt{N}}\right)^2}. \quad (6)$$

Clearly, we need an independent measure of p along with β from RICH.

1.4 Multiple Scattering Dominance

When multiple scattering is the dominant angular error (MSD limit), then momentum can be determined from the ring image width [8]. Since this method is new (or sufficiently old that it has been forgotten), we review the technique and its capabilities.

Historically, some early measurements of pion and muon masses in nuclear emulsions were based on this effect. In the experiment of Goldschmidt-Clermont *et al.* [9], secondary particles produced by primary cosmic-ray protons in emulsion were tracked (by human scanners looking through microscopes) and range was measured to find the particle kinetic energy via the Bethe-Bloch relation. They also measured the rms angular deflection of the track to obtain the momentum. Similar results were obtained by Camerini *et al.* [10] from multiple scattering and grain counting (recall that $dE/dx \propto 1/\beta^2$ at low energies).

If the angular width of the ring is multiple scattering (ms) dominated, the quadratic γ dependence of Eqs. (5) and (6) is reduced to first order since

$$\sigma_\theta = \sigma_\theta(\text{ms}) = \frac{k_{\text{ms}}}{p\beta} \sqrt{\frac{L}{X_0}} = \frac{k_{\text{ms}}}{m\gamma\beta^2} \sqrt{\frac{L}{X_0}}, \quad (7)$$

where $k_{\text{ms}} = (13.6/\sqrt{2}) \text{ MeV} = 9.6 \text{ MeV}$ and X_0 is the radiation length of the radiator medium [6]. Note that σ_θ is proportional to $1/p$; formally,

this is similar to particle bending in a magnetic field where the bending angle $\propto 1/p$. The strict similarity disappears when we insert the θ dependence of β and the (θ, N) dependence of L .

Combining Eqs. (2), (5), and (7), we obtain the momentum error of an MSD-RICH due to the β error [i.e., the second term of Eq. (5)]

$$\left(\frac{\sigma_p}{p}\right)_\beta = \frac{nK \cos^2 \theta}{m \sqrt{(\sin^2 \theta_n - \sin^2 \theta)}}, \quad (8)$$

where $\cos \theta_n = 1/n$ and $K \equiv nk_{ms}/\sqrt{(N_0 X_0)}$. Thus, for MSD and m known, Eq. (8) gives the momentum error due to the β error.

1.5 Momentum (without a Magnet) from Ring Radius and Width if L Is Known

In general, momentum is determined from multiple scattering by solving Eq. (7) for $p = [k_{ms}/\beta\sigma_\theta(ms)]\sqrt{(L/X_0)}$. Expressed in terms of the measured variables (θ, σ_θ) , we find

$$p = \frac{K' \cos \theta}{\sqrt{(\sigma_\theta^2 - \sigma_{\theta_0}^2)}}, \quad (9)$$

where $K' = nk_{ms}\sqrt{(L/X_0)}$ and we have deduced $\sigma_\theta(ms) \equiv \sqrt{(\sigma_\theta^2 - \sigma_{\theta_0}^2)}$, since σ_θ is the total measured ring width and σ_{θ_0} is the width from all momentum-independent sources. These include chromatic (E),

pixel (xyz), emission point (u_e), and impact parameter (v_e, w_e) errors but not multiple scattering (ms) or slowing (sl).

Here K' is required to be a known quantity; thus L must be known (or measured). This is the case for most RICH detectors where L is known from external tracking detectors, but for the LBL-RICH, L is not (and cannot be) directly measured. This case is treated in Sec. 1.6.

The mass defining kinematical relation $m = p/\beta\gamma$ may now be written in terms of the measured variables (θ, σ_θ) as

$$m = nK' \cos \theta \sqrt{\frac{\sin^2 \theta_n - \sin^2 \theta}{\sigma_\theta^2 - \sigma_{\theta_0}^2}}. \quad (10)$$

From Eqs. (9) and (10), we evaluate the momentum and mass errors as

$$\frac{\sigma_p}{p} = \sqrt{\frac{\frac{\epsilon^2}{2} + (\tan \theta \sigma_\theta)^2}{N}}, \quad (11)$$

$$\frac{\sigma_m}{m} = \sqrt{\frac{\frac{\epsilon^2}{2} + [(\gamma^2 + 1) \tan \theta \sigma_\theta]^2}{N}}, \quad (12)$$

where $\epsilon \equiv \sigma_\theta^2/(\sigma_\theta^2 - \sigma_{\theta_0}^2)$. Note that $\epsilon \approx 1$ for MSD while $\epsilon \gg 1$ for non-MSD. These derivations use the estimate of the width error [11], i.e.,

$$\sigma_{\sigma_\theta} = \frac{\sigma_\theta}{\sqrt{2N}}. \quad (13)$$

1.6 Momentum (without a Magnet) from Ring Radius and Width if N (not L) Is Known

Here, we consider the LBL-RICH case when L is not measured but only inferred from Eq. (2) as $L = N/(\epsilon_g \epsilon_a N_0 \sin^2 \theta)$, where ϵ_g is the geometrical efficiency for imaging the photons and ϵ_a is the absorption loss (see Sec. 3.5). The momentum defining relation, Eq. (7), may now be written in terms of the measured variables (θ, σ_θ, N) as

$$p = \left(\frac{K}{\tan \theta} \right) \sqrt{\frac{N}{(\sigma_\theta^2 - \sigma_{\theta 0}^2) \epsilon_g \epsilon_a}}, \quad (14)$$

where again $K = nk_{ms}/\sqrt{(N_0 X_0)}$. The mass equation $m = p/\beta\gamma$ now expressed in terms of the same variables (θ, σ_θ, N) is

$$m = \left(\frac{nK}{\tan \theta} \right) \sqrt{\left(\frac{\sin^2 \theta_n - \sin^2 \theta}{\sigma_\theta^2 - \sigma_{\theta 0}^2} \right) \frac{N}{\epsilon_g \epsilon_a}}, \quad (15)$$

thus from Eqs. (14) and (15), we obtain for the momentum and mass errors

$$\frac{\sigma_p}{p} = \sqrt{\frac{\frac{1}{4} + \frac{\epsilon^2}{2} + \left(\frac{\tan \theta \sigma_\theta}{\sin^2 \theta} \right)^2}{N}}, \quad (16)$$

$$\frac{\sigma_m}{m} = \sqrt{\frac{\frac{1}{4} + \frac{\epsilon^2}{2} + \left[\left(\gamma^2 + \frac{1}{\sin^2 \theta} \right) \tan \theta \sigma_\theta \right]^2}{N}}, \quad (17)$$

where negligible errors are assumed for ϵ_g and ϵ_a (see Sec. 3.5). Note that the resolutions of Eqs. (11) and (12) are only marginally better than Eqs. (16) and (17); thus, little is lost by not having tracking detectors inside the water. In fact, we have not found a reasonable way to implement a tracker without seriously compromising the RICH imagery. Luckily, Eqs. (16) and (17) show that the impossible is also unnecessary. Note that for MSD, the first two terms in the numerator of Eq. (16) are 3/4 and the third term is negligible, so that $\sigma_p/p \approx 0.87/\sqrt{N}$. With $N \approx 850$ image points (or even half that many), the $1/\sqrt{N}$ term is small, i.e., 3–5%, thus indicating that good momentum resolution is possible, in principle.

2. Experimental Layout

The layout of Fig. 1 shows the radiator, mirror, and detector array. The mirror center of curvature C fixes the origin (0, 0, 0) of the ZXY coordinate system. The water volume starts at $z = 0$ and extends to $z = 30$ m and transversely to $x = \pm 15$ m, and $y = \pm 15$ m. A spherical mirror of curvature $r_m = 30$ m is placed at the far end of the cube, i.e., at $z = 30$ m.

The optimal detector sphere for tracks uniformly distributed in the water volume ($0 \leq z \leq r_m$) is at $z = (r_m/2)\sqrt{1+(3\sin^2\theta/4)} = 17.3$ m; thus the PM's could be arrayed on a spherical surface 17.3 m into the water target, hence 12.7 m upstream of the mirror. In fact, the PM's will be arrayed on a flat plane at $z = 17.3$ m because, in the case of a spherical array, too many photons are lost to the side walls. The PM's should cover 20% of the 30×30 m² surface, i.e., 180 m² with a pixel size of 125 mm, i.e., 14 400 PM's on a grid of 250 mm pitch. A coincidence of ≥ 100 PM hits in a 128 ns gate during the 6 μ s SPS burst window (see Sec. 5.1) will signal an interesting event and start readout. The PM's will be read out with seven-bit TDC's or FADC's for a period of 128 ns in bins of 1 ns, thus increasing the detector granularity to 1.8 Mpixels, quite enough to image events of maximum size $N \leq 2 \times 10^4$.

In order to reduce the cost and increase the number of pixels, we are designing 254 mm diameter HPD's [12, 13], each with 36 pads of size 36×36 mm² at the photocathode surface (and 9×9 mm² at the silicon wafer plane). A total of 3600 of these HPD's will be needed containing 129 600 pixels. Experiments have shown that ≤ 1 ns timing can be obtained from HPD's if the pad signals are independently brought out of the vacuum envelope and treated by conventional fast electronics [14].

The mirror radius is chosen relatively small ($r_m = 30$ m, $f = r_m/2 = 15$ m) so that the image radius [$r_{\text{image}} \approx f\theta \approx (15 \text{ m})(0.72) = 10.8$ m] is mostly contained (with geometric efficiency ϵ_g) inside the ± 15 m PM (or

HPD) array. Because the detector array is 80% transparent, the water volume can be extended into the good optics region 17.3 m upstream of the detector surface. Photons from this region will be detected with 16% effective coverage rather than 20%.

A hadron track of pathlength 1λ (one absorption length in water is 850 mm) will make an image with $N \approx 850\epsilon_g\epsilon_a$ hit points. The latter factor $\epsilon_a = e^{-\mu\ell}$ is the efficiency for photon transmission in pathlength ℓ of water ($\langle\ell\rangle \approx 30$ m in the LBL-RICH). Water transparency with $\mu^{-1} > 100$ m has been attained for 3.9 eV photons [15], whereas the LBL-RICH photon detection range is only from 2.5 to 3.5 eV.

The momentum range for MSD extends up to about 4.5 GeV/c. This range includes almost all hadrons produced by 1 to 20 GeV neutrinos via quasi-elastic (QEL) and deep inelastic scattering (DIS) via charged and neutral current interactions. The threshold momentum for Cherenkov radiation in water is $p = 1.12m$, hence 0.12, 0.16, 0.55, and 1.05 GeV/c for muons, pions, kaons, and protons, respectively. About 25% of the protons from quasi-elastic interactions are above the proton threshold. Generally, all above threshold hadrons will have their direction, momentum, velocity, mass, and $(Ze)^2$ measured in the LBL-RICH.

Electrons and gammas can also be measured because EM shower electrons in water ($X_0 = 36$ cm) radiate if $p > 0.57$ MeV/c. A Cherenkov sensitive shower is therefore somewhat shorter than a dE/dx sensitive shower and is less affected by low-energy fluctuations. Since it is fully contained in about 5 m, we take 25 m as the fiducial target length thus

defining the LBL-RICH fiducial mass as 22.5 kt. The shower produces a more diffuse, but still identifiable, ring ($\sigma_\theta \approx 50$ mrad) than a hadron ring ($\sigma_\theta \leq 15$ mrad) but with many more points, i.e., $N \approx 3000 \epsilon_g \epsilon_a E_e$ (GeV). The water acts as the showering medium and radiator of a homogeneous Cherenkov calorimeter with resolution $\sigma_{E_e}/E_e \approx 8.5\%/\sqrt{E_e}$ (GeV). The direction of the particle initiating the EM shower is accurately determined by the ring center to better than 1 mrad.

Muon identification is obtained for $p \leq 1.5$ GeV/c by direct measurement of β and p (from MSD) which determines m with error σ_m from 3 to 6 MeV, sufficient to distinguish muons and pions. Above 1.5 GeV/c, σ_m becomes larger than 10 MeV, and muon identification by this method is not possible, but then the muon range is so long that the image "lights up like a muon sign." For example, a 1.1 GeV/c muon with 5 m range in water will make a ring with 5000 $\epsilon_g \epsilon_a$ image points compared to 800 $\epsilon_g \epsilon_a$ for a 1λ pathlength pion. The measurement of p for muons is also good, i.e., $\sigma_p/p \leq 6\%$ for $p \leq 4.5$ GeV/c. It becomes limited by emission point errors $\sigma_\theta(z_e)$ due to the long muon pathlength in water. Extension to higher momentum (i.e., $\sigma_p/p \approx 10\%$ for $p = 15$ GeV/c) can be attained by time slicing the track into a series of shorter segments.

The capability of the LBL-RICH is such that it can explore values of L/E_ν between 50 and 700 km/GeV with a broad band neutrino beam of energy E_ν between 1 and 15 GeV at Gran Sasso ($L = 732$ km). In neutrino disappearance ($\mu \rightarrow \tau$) and neutrino appearance ($\mu \rightarrow e$)

experiments with broad band beams, it is essential to accurately determine E_ν . This is possible in LBL-RICH because the direction and energy of muons and electrons are well-measured as, indeed, are the hadrons.

2.1 Particle Momentum Resolution

The contributions to the angular error σ_θ vs impact parameter ρ_e (relative to C) for a 1 GeV/c pion with an 850 mm pathlength in water are shown in Fig. 2 for the detector layout of Fig. 1. Note that the dominant contribution is from multiple scattering $\sigma_\theta(ms) = 15$ mrad, while chromatic $\sigma_\theta(E) = 3.6$ mrad, pixel $\sigma_\theta(xyz) = 1.9$ mrad, and slowing $\sigma_\theta(sl) = 0.4$ mrad are less important. Only the impact parameter errors $\sigma_\theta(v_e)$, $\sigma_\theta(w_e)$, and emission point error $\sigma_\theta(u_e)$ vary with $\rho_e = \sqrt{(v_e^2 + w_e^2)}$, but they are not significant even for ρ_e as large as 15 m.

We have evaluated the resolutions σ_p/p and σ_m for $\theta_p = 0$ tracks and pixel sizes $\Delta x = \Delta y = 125$ mm, $\Delta z = 1$ mm, $\Delta u_e = 850$ mm, $\Delta v_e = \Delta w_e = 100$ mm, and $\Delta\theta_p = \Delta\phi_p = 1$ mrad. The refractive index and dispersion $n(E)$ of water were obtained from Ref. [16].

Figure 3 shows the resolution σ_p/p vs p for 15 m pathlength muons or for 0.85 m pathlength hadrons (π , K, P). The solid curves are from multiple scattering [Eq. (16)] while the dot-dash curves are from velocity β when m is known [(Eq. (8))]. Note that the solid curves are everywhere excellent, i.e., $1 < \sigma_p/p < 6\%$ for $p \leq 5$ GeV/c. For K's and P's, the dot-dash curves are everywhere $< 1\%$ and better than the solid

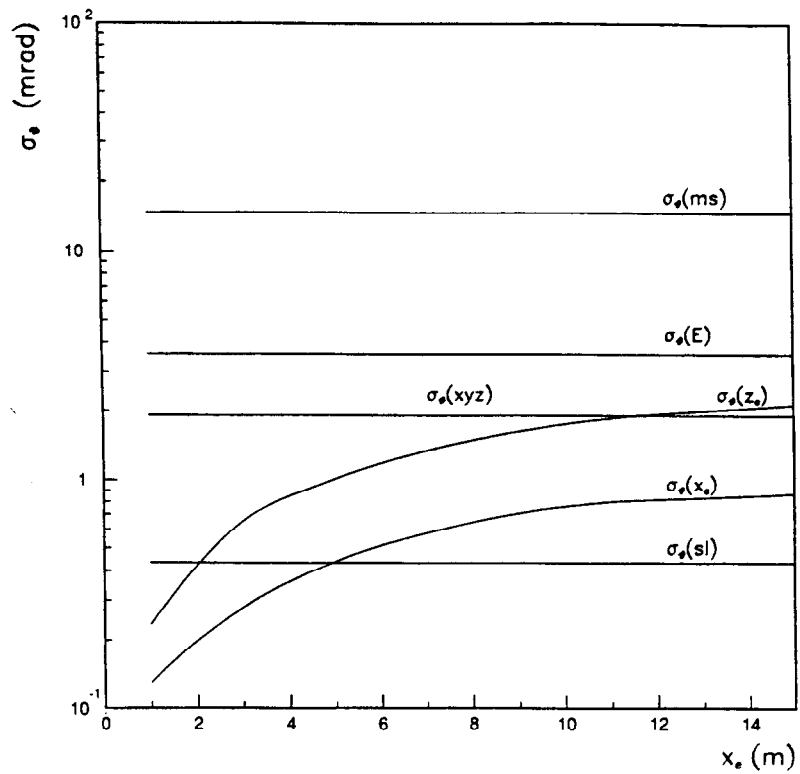


Fig. 2. The Cherenkov angle width vs impact parameter ρ_e for a 1 GeV/c pion track 85 cm long in water. The contributions shown are $\sigma_\theta(ms)$ from multiple scattering, $\sigma_\theta(E)$ chromatic, $\sigma_\theta(xyz)$ from pixel size, $\sigma_\theta(sl)$ from energy loss, $\sigma_\theta(z_e)$ from tracklength, and $\sigma_\theta(x_e)$ from impact parameter.

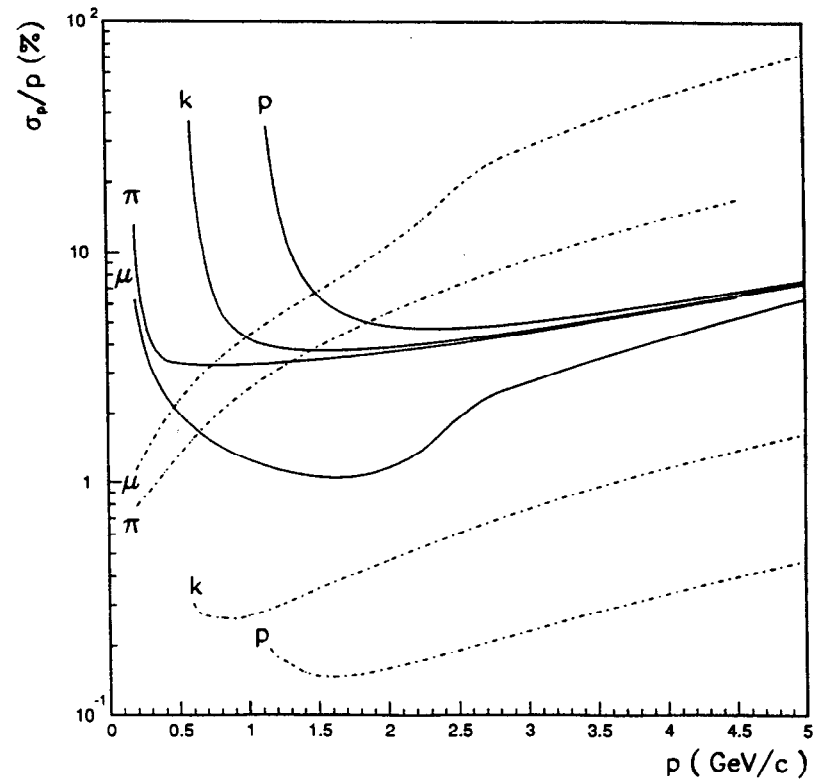


Fig. 3. The resolution σ_p/p vs p for (μ , π , K, P) in water and the geometry of Fig. 1. The solid curves are from multiple scattering [Eq. (16)], whereas the dot-dash curves are from the β measurement [Eq. (8)] assuming mass is known.

curves, whereas for π 's and μ 's, they are only better for $p < 1.3$ and $0.5 \text{ GeV}/c$, respectively.

Figure 4 shows the mass resolution σ_m/m from combined σ_θ and β measurements, i.e., Eq. (17). For $p \leq 1.25 \text{ GeV}/c$, the resolution $\sigma_m \approx 5\text{--}7 \text{ MeV}$ is sufficient for μ/π identification. Above $1 \text{ GeV}/c$, the muon pathlength becomes so long that the muon is identified by its large N (i.e., $N > 5000 \epsilon_g \epsilon_a$). The K mass resolution, $\sigma_m \approx 20\text{--}30 \text{ MeV}$ for $p < 5 \text{ GeV}/c$, is sufficient for π/K identification and the P mass resolution, $\sigma_m \approx 50\text{--}60 \text{ MeV}$ for $p < 5 \text{ GeV}/c$, is also sufficient for K/P identification. Therefore, the combined σ_θ and β measurements determine the identification of all stable particles and allows us to choose the best resolution curves of Fig. 3 (solid or dot-dash).

2.2 Particle Direction Determination

The polar angles (θ_p, ϕ_p) of a particle producing a ring image are determined with high precision from the ring center, i.e., $\sigma_{\theta_p} \approx \sigma_{\phi_p} \approx \sigma_\theta/\sqrt{N}$. For a $1 \text{ GeV}/c$ pion track in water with Cherenkov pathlength of 85 cm , we have $\sigma_\theta \approx 15 \text{ mrad}$ and for $N \approx 400$, then $\sigma_{\theta_p} \approx \sigma_{\phi_p} \approx 0.75 \text{ mrad}$. The direction error for electrons, gammas, and muons should be at least as good because N is considerably larger.

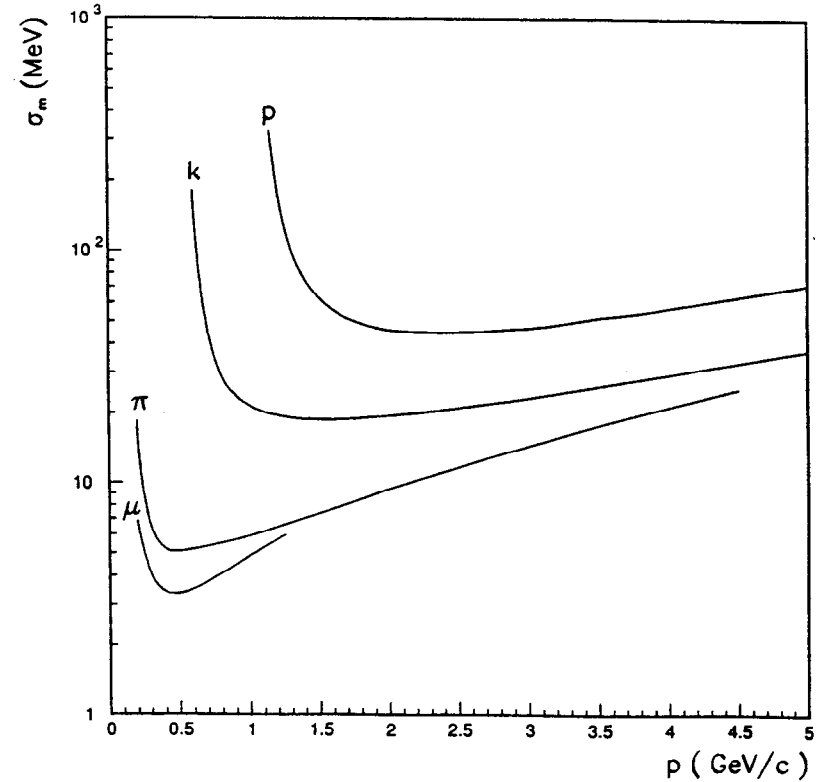


Fig. 4. The mass resolution σ_m vs p for (μ, π, K, P) in water and geometry of Fig. 1. The solid curves [Eq. (17)] are from combined measurements of multiple scattering and β .

2.3 Quasi-Elastic Neutrino Interactions

Here, we show events due to 12 GeV/c neutrinos interacting quasi-elastically to produce leptons (ℓ) via the process ($\nu_\ell + N \rightarrow \ell + P$) at random points in the water volume (see Fig. 1). The events were obtained from a PYTHIA 5.7 simulation with all fast decays allowed. They were subsequently introduced into GEANT to simulate the tracks with multiple scattering, energy loss, secondary interactions, and Cherenkov light emission. The PM hit points are labeled as muons, electrons (or gammas), protons, and pions. All images contain only 10% of the expected photoelectron hit points because of computer memory limitations.

- In Figs. 5–7, we show three successive events of the type $\nu_\mu + N \rightarrow \mu^- + P$.
- Figures 8–10 show three successive events of the type $\nu_e + N \rightarrow e^- + P$. The electrons were allowed to interact; thus the images shown are due to showers.
- Figures 11–14 show four successive events of the type $\nu_\tau + N \rightarrow \tau^- + P$. The τ^- 's were allowed to decay naturally via the dominant e^- , μ^- , ρ^- , or π^- branching modes.

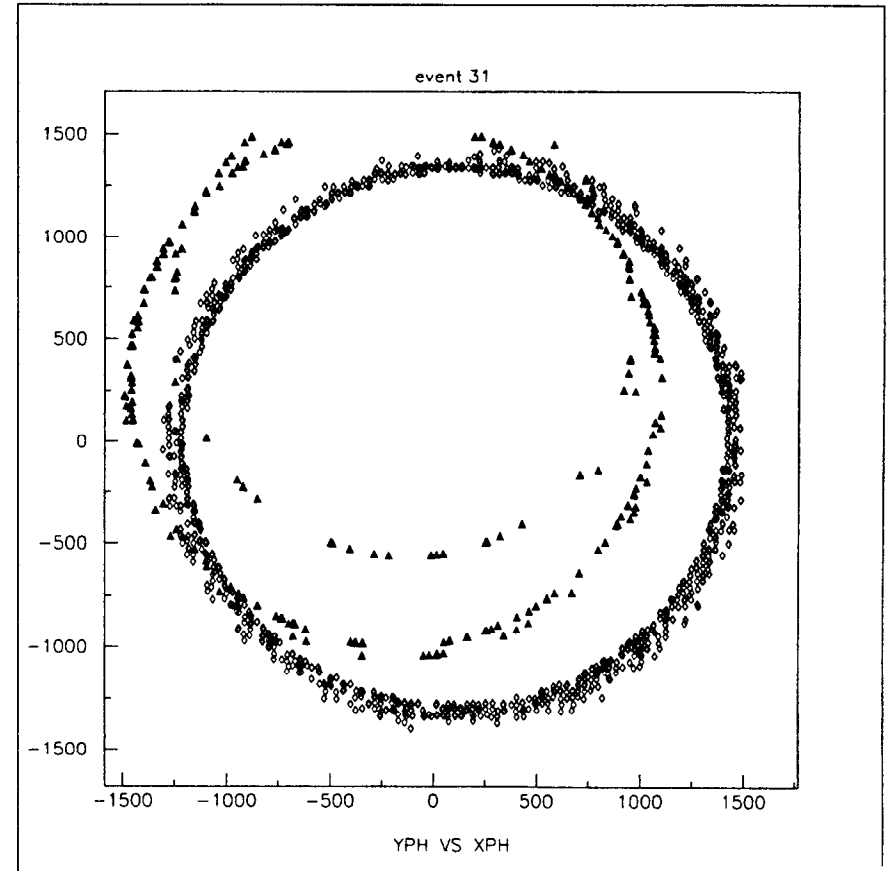


Fig. 5. A Monte Carlo simulation of a quasi-elastic event (#31) $\nu_\mu + N \rightarrow \mu^- + P$ for $E_{\nu\mu} = 12$ GeV. It has two proton rings (black triangles) (the smaller one is due to a scatter) and one very dense muon ring (open diamonds). Muon identification here is obvious. The diffuseness of the image is due to the long muon pathlength; thus emission point errors dominate. This effect can be removed by time slicing the image (thus breaking the track up into a series of shorter segments) and reconstructing each segment.

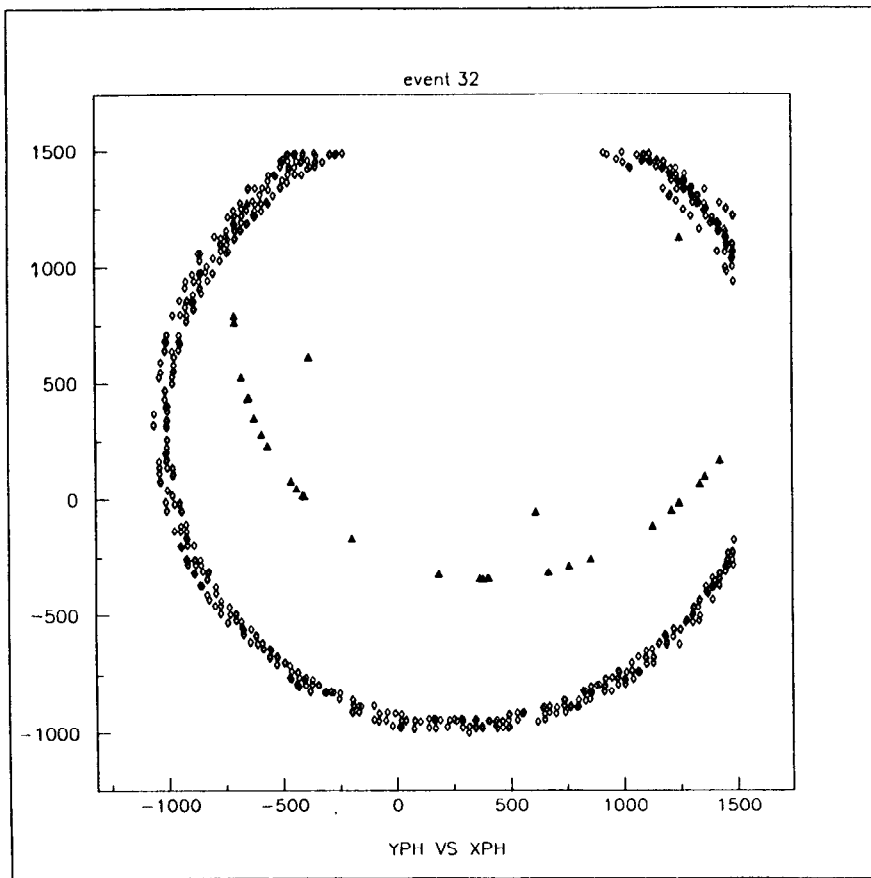


Fig. 6. A Monte Carlo simulation of a quasi-elastic event (#32) $\nu_{\mu} + N \rightarrow \mu^{-} + P$ for $E_{\nu_{\mu}} = 12$ GeV. It shows one proton ring (black triangles) with a hint of a second (it is evident if all N hits are plotted) along with a self-evident muon ring (open diamonds).

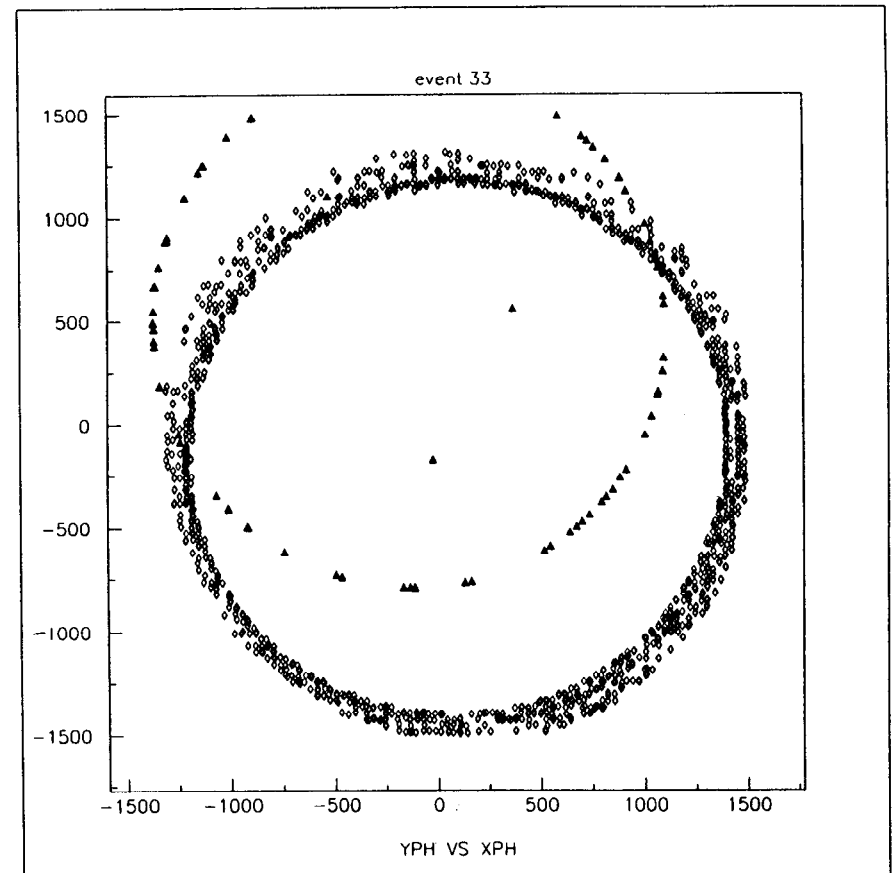


Fig. 7. A Monte Carlo simulation of a quasi-elastic event (#33) $\nu_{\mu} + N \rightarrow \mu^{-} + P$ for $E_{\nu_{\mu}} = 12$ GeV. It shows one proton ring (black triangles) with some extra hits (a second proton ring due to a scatter) and one muon ring (open diamonds). The rings are reasonably easy to identify (by eye) and so the pattern recognition algorithm will surely work.

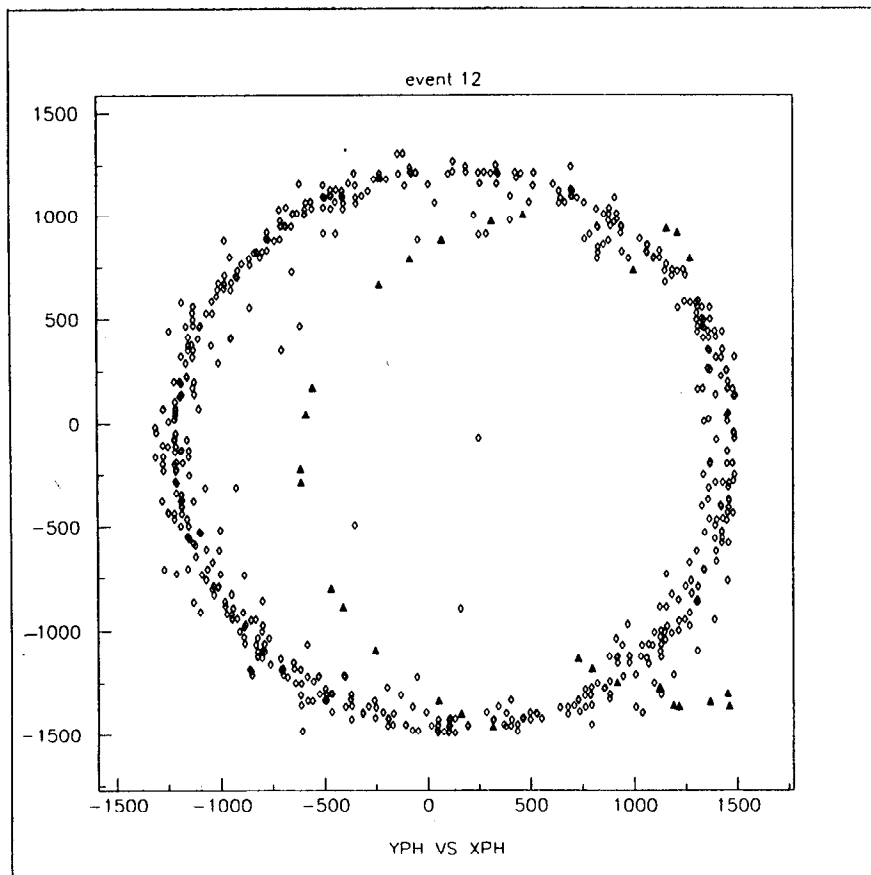


Fig. 8. A Monte Carlo simulation of a quasi-elastic event (#12) $\nu_e + N \rightarrow e^- + P$ with $E_{\nu_e} = 12$ GeV. It has one proton ring (black triangles) (plus a scatter which may be resolvable) and one dense electron ring (open diamonds). Electron identification and energy measurement should be good.

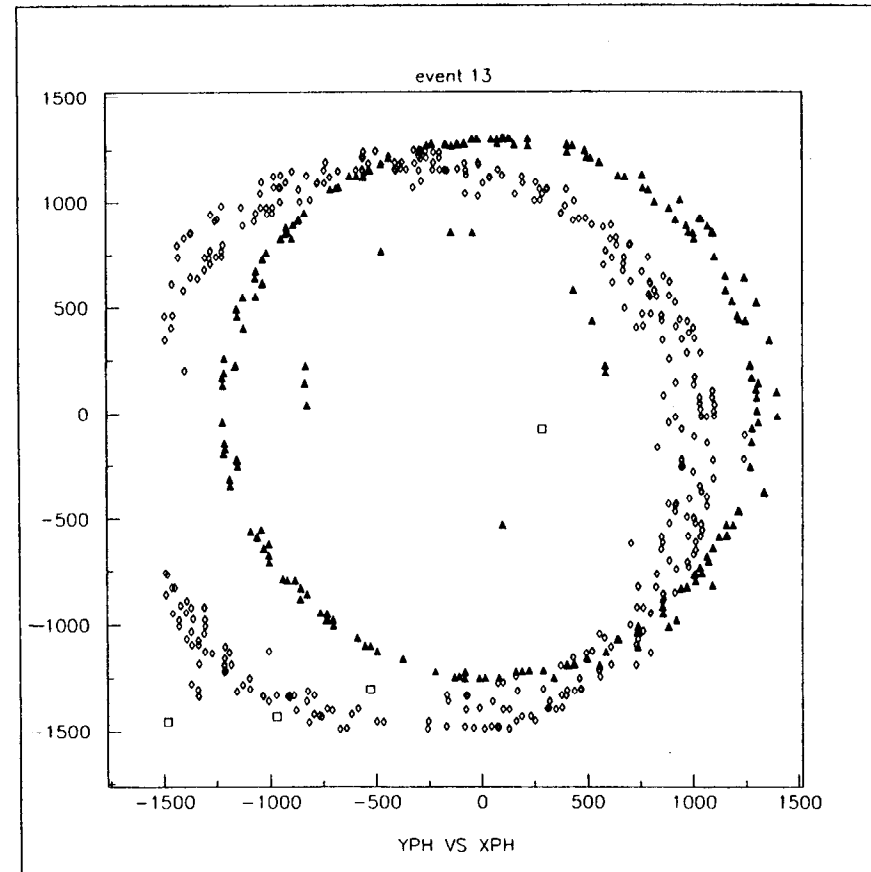


Fig. 9. A Monte Carlo simulation of a quasi-elastic event (#13) $\nu_e + P \rightarrow e^- + \Delta^{++}$ and $\Delta^{++} \rightarrow P + \pi^+$ for $E_{\nu_e} = 12$ GeV. It shows two proton rings (black triangles) and one electron ring (open diamonds). There is a hint of a pion ring (open squares) which is evident if all N hits are plotted.

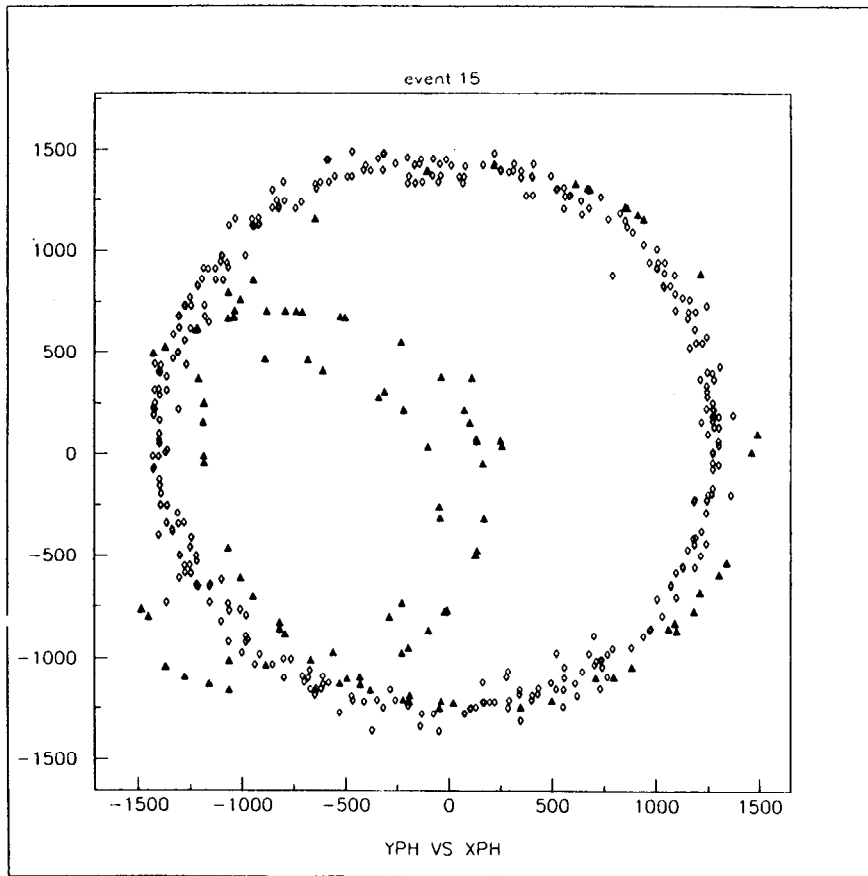


Fig. 10. A Monte Carlo simulation of a quasi-elastic event (#15) $\nu_e + N \rightarrow e^- + P$ for $E_{\nu_e} = 12$ GeV. It has three proton rings (black triangles) (the smaller ones are due to scatterings) and one electron ring (open diamonds).

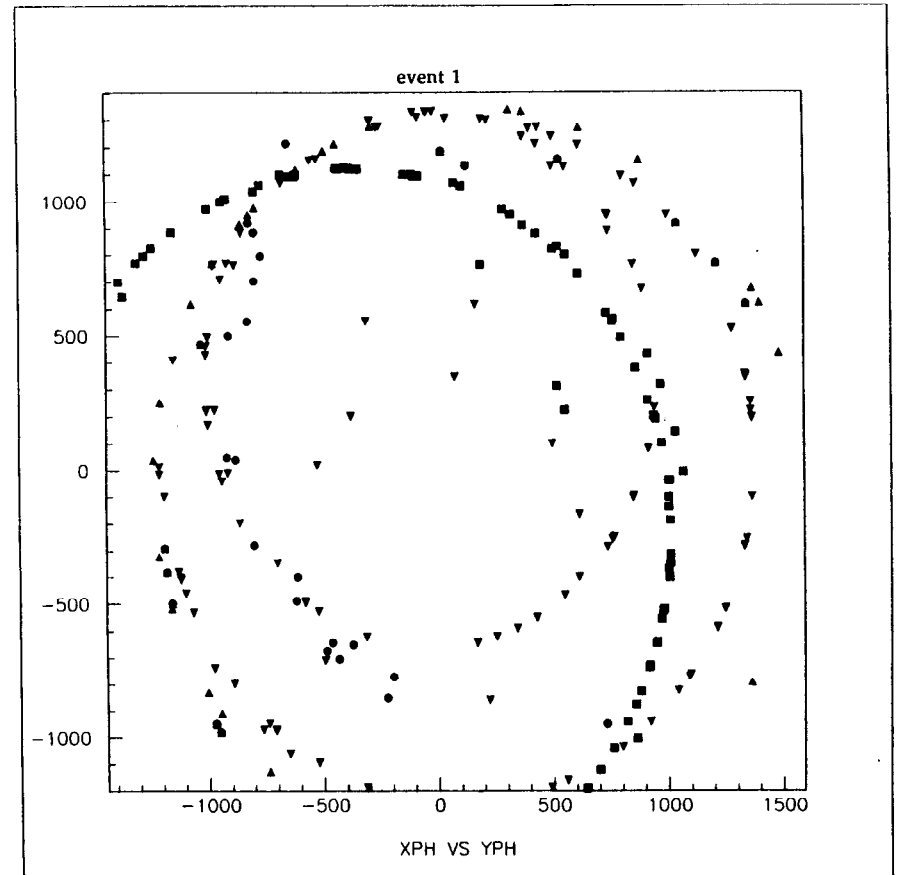


Fig. 11. A Monte Carlo simulation of a quasi-elastic event (#1) $\nu_\tau + N \rightarrow \tau + P$ for $E_{\nu_\tau} = 12$ GeV. It shows two proton rings (black triangles) and one electron ring (black circles), and one or two pion rings (black squares). Clearly, this event would be challenging.

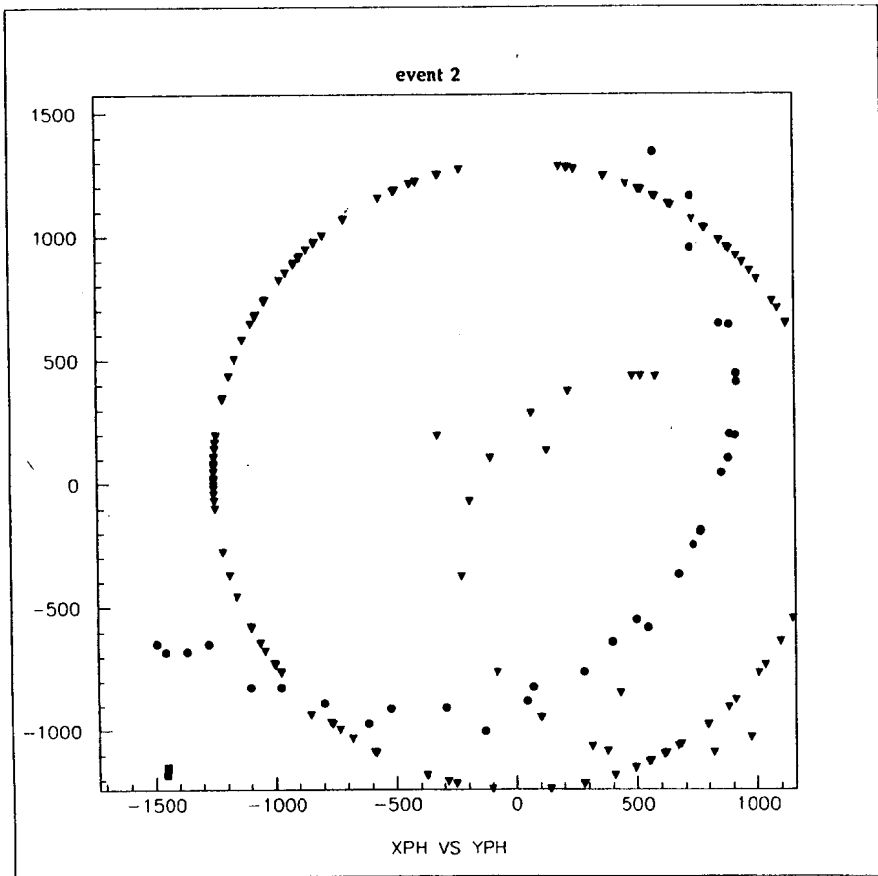


Fig. 12. A Monte Carlo simulation of a quasi-elastic event (#2) $\nu_\tau + N \rightarrow \tau + P$ for $E_{\nu\tau} = 12$ GeV. It shows two proton rings (black triangles) and one electron ring (black circles).

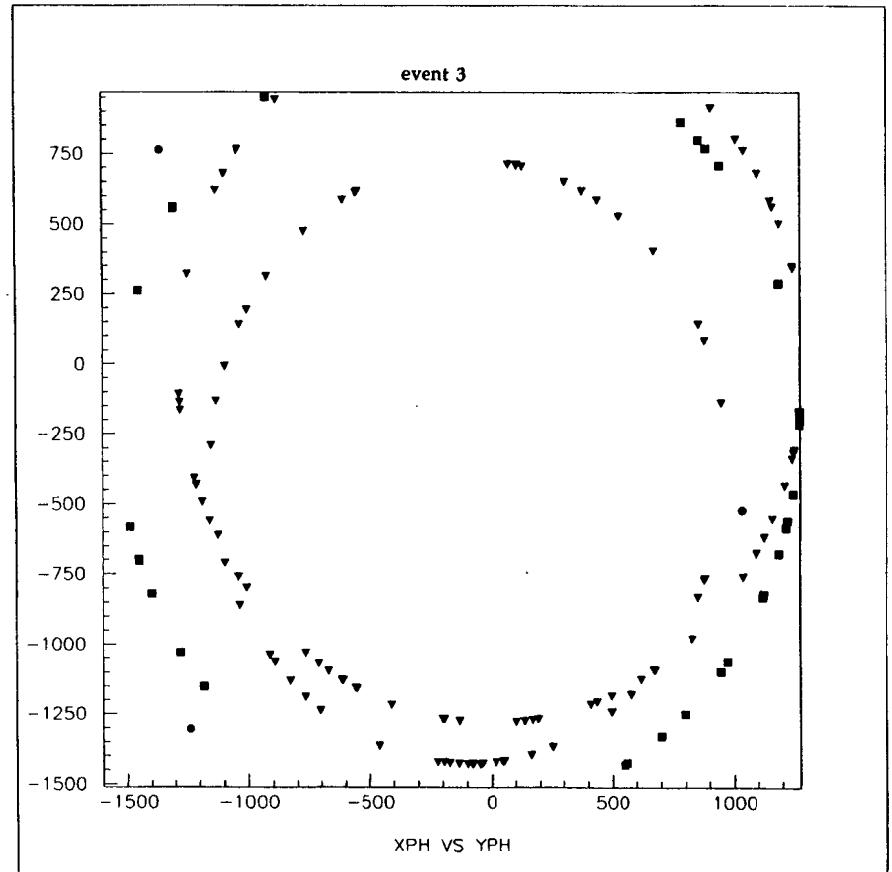


Fig. 13. A Monte Carlo simulation of a quasi-elastic event (#3) $\nu_\tau + N \rightarrow \tau + P$ for $E_{\nu\tau} = 12$ GeV. It shows two proton rings (black triangles) and one pion ring (black squares) with a hint of an electron ring (black circles).

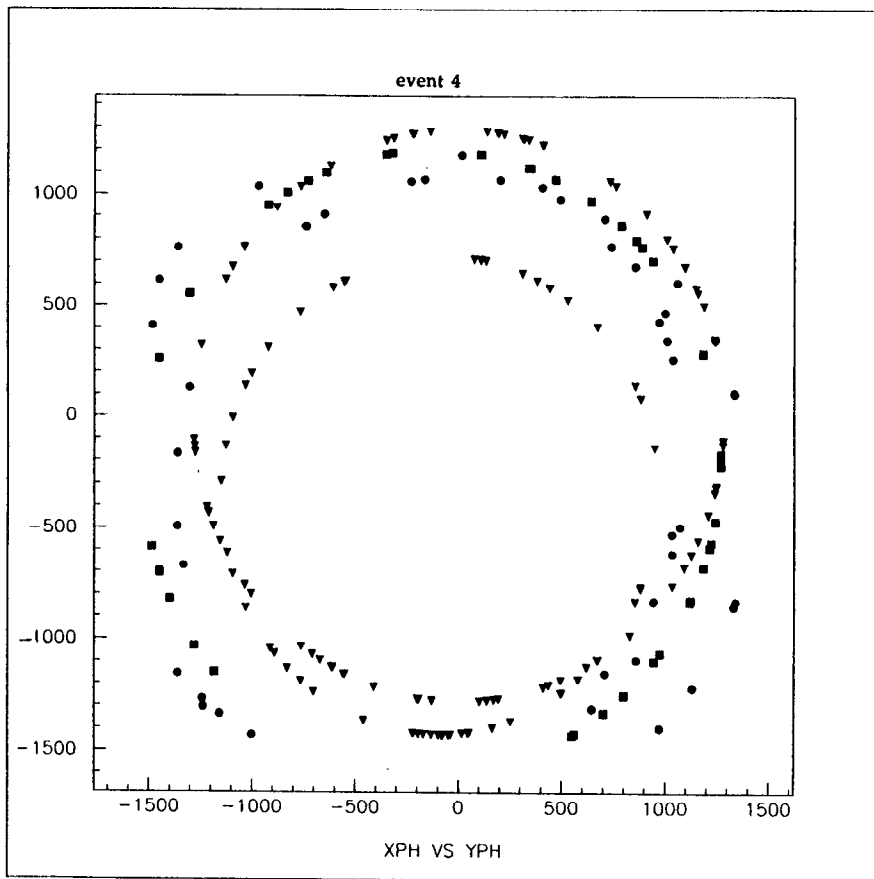


Fig. 14. A Monte Carlo simulation of a quasi-elastic event (#4) $\nu_\tau + N \rightarrow \tau + P$ for $E_{\nu_\tau} = 12$ GeV. It shows two proton rings (black triangles) and two electron rings (black circles), and one pion ring (black squares). Clearly, this event would be challenging.

3. Properties of Ring Images

Every charged particle above Cherenkov threshold makes a ring image. Neutrals which decay into charged pairs also form images. Electrons and gammas will shower and produce somewhat more diffuse images.

Because Cherenkov light rays form parallel bundles in all planes containing the track and because spherical mirrors focus parallel bundles to a point on the focal surface, hence the contributions from all planes combine to form a ring. This means that parallel tracks form the same ring and that the ring center determines the particle direction (θ_p, ϕ_p) [7].

3.1 Parameters of the Image

The ring image is characterized by nine parameters: three detected photon coordinates (z, x, y) ; and five track parameters, i.e., the photon emission point (u_e, v_e, w_e) and the particle direction (θ_p, ϕ_p) , and a single parameter for photon energy E . The photon emission point u_e is measured along the particle track, and the impact parameter $\rho_e = \sqrt{(v_e^2 + w_e^2)}$ is the perpendicular distance to the track from the mirror center of curvature C .

We define two different coordinate systems (see appendix Fig. A1), the ZXY system, fixed relative to the mirror and the water tank (Fig. 1), with unit vectors $(\vec{k}, \vec{i}, \vec{j})$ and the PQR system, fixed to each track and

defined from C such that P is parallel, Q and R are normal to the track, with unit vectors $(\bar{a}_p, \bar{b}_p, \bar{c}_p)$. The photon emission point is (z_e, x_e, y_e) in the ZXY system and (u_e, v_e, w_e) in the PQR system. The photon detection point is (z, x, y) in the ZXY system and (u, v, w) in the PQR system. A particle tracker, if available, would measure (u_e, v_e, w_e) , whereas the photon detector will measure (z, x, y) . Note that (z, x, y) and (z_e, x_e, y_e) are independent of (θ_p, ϕ_p) while (u, v, w) and (u_e, v_e, w_e) depend on (θ_p, ϕ_p) .

Seven of the nine variables, i.e., $\zeta_i = (z, x, y, v_e, w_e, \theta_p, \phi_p)$, can be determined with arbitrary precision. The group (z, x, y) depend on the accuracy of the photon detector while $(v_e, w_e, \theta_p, \phi_p)$ depend on the accuracy of the presumed tracker. In case of the LBL-RICH, these are found by the procedure developed below. The error in θ , due to errors in the variables ζ_i , may be expressed as

$$\sigma_\theta(\zeta_i) = \left(\frac{\partial \theta}{\partial \zeta_i} \right) \sigma_{\zeta_i}, \quad (18)$$

where $\partial \theta / \partial \zeta_i$ is calculated from the reconstruction relation $\theta = \theta(\zeta_i)$. Analytic forms for $\sigma_\theta(\zeta_i)$ evaluated from $\theta = \theta(\zeta_i)$ may be found in Ref. [7] and more generally in Appendix A.

In contrast, the photon emission point u_e along the track has an intrinsic error

$$\sigma_{u_e} = \frac{\Delta u_e}{\sqrt{12}} \quad (19)$$

limited by the radiator pathlength Δu_e ; however, in a focused system $\partial \theta / \partial u_e = 0$ (or is small even for large values of ρ_e); thus $\sigma_\theta(u_e)$ is never dominant. Similarly, the photon energy error for a square detector response is

$$\sigma_E = \frac{\Delta E}{\sqrt{12}}, \quad (20)$$

which can be reduced only by reducing the detector energy bandwidth ΔE . The corresponding Cherenkov angle error is

$$\sigma_\theta(E) = \left(\frac{\partial \theta}{\partial n} \right) \left(\frac{dn}{dE} \right) \sigma_E, \quad (21)$$

where $n(E)$ is the radiator dispersion function. These errors define the limits of the RICH resolution.

An important advantage of RICH is that the Cherenkov angle distributions are Gaussian, without the Landau tail which characterizes dE/dx (energy loss) detectors.

3.2 Impact Parameter, Vertex, and Emission Point Vectors and Cherenkov Angle

The unit vector \bar{a}_p along the track, parallel to P (see Fig. A1), has ZXY components

$$\begin{aligned}
\bar{a}_p &= a_{pz}\bar{k} + a_{px}\bar{i} + a_{py}\bar{j}, \\
a_{pz} &= \cos\theta_p, \\
a_{px} &= \sin\theta_p \cos\phi_p, \\
a_{py} &= \sin\theta_p \sin\phi_p.
\end{aligned} \tag{22}$$

The unit vector \bar{b}_p along Q has components in ZXY

$$\begin{aligned}
\bar{b}_p &= b_{pz}\bar{k} + b_{px}\bar{i} + b_{py}\bar{j}, \\
b_{pz} &= -a_{px}, \\
b_{px} &= \sin^2\phi_p + \cos\theta_p \cos^2\phi_p \equiv \varepsilon_x, \\
b_{py} &= (\cos\theta_p - 1)\cos\phi_p \sin\phi_p \equiv \eta.
\end{aligned} \tag{23}$$

The unit vector $\bar{c}_p = \bar{a}_p \times \bar{b}_p$ along R is normal to \bar{a}_p and \bar{b}_p with ZXY components

$$\begin{aligned}
\bar{c}_p &= c_{pz}\bar{k} + c_{px}\bar{i} + c_{py}\bar{j}, \\
c_{pz} &= -a_{py}, \\
c_{px} &= \eta, \\
c_{py} &= \cos^2\phi_p + \cos\theta_p \sin^2\phi_p \equiv \varepsilon_y.
\end{aligned} \tag{24}$$

Thus, $(\bar{k}, \bar{i}, \bar{j})$ and $(\bar{a}_p, \bar{b}_p, \bar{c}_p)$ are the unit vectors of the ZXY and PQR coordinate systems, respectively. The specific choice of QR axes is made such that $\bar{a}_p \rightarrow \bar{k}$, $\bar{b}_p \rightarrow \bar{i}$, $\bar{c}_p \rightarrow \bar{j}$ as $\theta_p \rightarrow 0$.

The particle production (neutrino interaction) vertex \bar{r}_v has ZXY components (z_v, x_v, y_v) and PQR components (u_{va}, v_e, w_e) , where

$$\begin{aligned}
\bar{r}_v &= z_v\bar{k} + x_v\bar{i} + y_v\bar{j} = u_{va}\bar{a}_p + v_e\bar{b}_p + w_e\bar{c}_p, \\
u_{va} &= \bar{r}_v \cdot \bar{a}_p, \\
v_e &= \bar{r}_v \cdot \bar{b}_p, \\
w_e &= \bar{r}_v \cdot \bar{c}_p.
\end{aligned} \tag{25}$$

The impact parameter \bar{r}_{ip} is that vector normal to \bar{a}_p which when added to a vector proportional to \bar{a}_p gives the vertex vector \bar{r}_v ; thus

$$\begin{aligned}
\bar{r}_{ip} &= \bar{r}_v - (\bar{r}_v \cdot \bar{a}_p)\bar{a}_p = v_e\bar{b}_p + w_e\bar{c}_p = z_{ip}\bar{k} + x_{ip}\bar{i} + y_{ip}\bar{j}; \\
z_{ip} &= \sin\theta_p [z_v \sin\theta_p - (x_v \cos\phi_p + y_v \sin\phi_p)\cos\theta_p]; \\
x_{ip} &= -z_v \sin\theta_p \cos\theta_p \cos\phi_p + x_v(1 - \sin^2\theta_p \cos^2\phi_p) - y_v \sin^2\theta_p \sin\phi_p \cos\phi_p; \\
y_{ip} &= -z_v \sin\theta_p \cos\theta_p \sin\phi_p - x_v \sin^2\theta_p \sin\phi_p \cos\phi_p + y_v(1 - \sin^2\theta_p \sin^2\phi_p).
\end{aligned} \tag{26}$$

where the second equality of the top equation of Eq. (25) identifies v_e and w_e as impact parameters. In Ref. [7], ϕ_p was explicitly set to zero by a rotation, and only v_e was considered (they are called x_e). This is equivalent to setting $y_v = 0$ as is shown by considering the ZXY components of \bar{r}_{ip} in the limit $\phi_p \rightarrow 0$, i.e., $z_{ip} \rightarrow A \sin\theta_p$, $x_{ip} \rightarrow -A \cos\theta_p$ (here $A \equiv z_v \sin\theta_p - x_v \cos\theta_p$), and $y_{ip} \rightarrow y_v$; thus $y_{ip} = 0$ only if $y_v = 0$.

Therefore, the geometry of Ref. [7] is not completely general because it implicitly assumes $y_v = 0$ and uses only one impact parameter v_e ; whereas in general, $y_v \neq 0$ and two impact parameters v_e and w_e are required. The formulation and reconstruction method given below is, however, quite general. The derivatives found in

Ref. [7] apply only for $y_v = 0$ and should be replaced by the more general ones given in Appendix A.

In ZXY, the photon emission point is (z_e, x_e, y_e) ; thus $\vec{r}_e = z_e \vec{k} + x_e \vec{i} + y_e \vec{j}$ with $r_e = \sqrt{(z_e^2 + x_e^2 + y_e^2)}$. In PQR, the emission point is at distance u_{ve} along \vec{a}_p from \vec{r}_v , i.e.,

$$\vec{r}_e = \vec{r}_v + u_{ve} \vec{a}_p = u_e \vec{a}_p + v_e \vec{b}_p + w_e \vec{c}_p \quad (27)$$

with $r_e = \sqrt{(u_e^2 + v_e^2 + w_e^2)}$ and the second equality stemming from Eq. (25) with $u_e = u_{va} + u_{ve}$. Since the (z_e, x_e, y_e) coordinates are defined in ZXY, they are obviously independent of (θ_p, ϕ_p) . The PQR components (u_e, v_e, w_e) , expressed in terms of (z_e, x_e, y_e) and (θ_p, ϕ_p) , are

$$\begin{aligned} u_e &= z_e a_{pz} + x_e a_{px} + y_e a_{py}, \\ v_e &= z_e b_{pz} + x_e b_{px} + y_e b_{py}, \\ w_e &= z_e c_{pz} + x_e c_{px} + y_e c_{py}. \end{aligned} \quad (28)$$

and

$$\begin{aligned} z_e &= u_e a_{pz} + v_e b_{pz} + w_e c_{pz}, \\ x_e &= u_e a_{px} + v_e b_{px} + w_e c_{px}, \\ y_e &= u_e a_{py} + v_e b_{py} + w_e c_{py}. \end{aligned} \quad (29)$$

In matrix notation, $u_e = A z_e$ and $z_e = B u_e$ where u_e and z_e are column vectors $(u_e, v_e, w_e)^T$, $(z_e, x_e, y_e)^T$. Here A is the matrix with $a_{11} = a_{pz}$, $a_{12} = a_{px}$, $a_{13} = a_{py}$, $a_{21} = b_{pz}$, $a_{22} = b_{px}$, $a_{23} = b_{py}$, $a_{31} = c_{pz}$, $a_{32} = c_{px}$, $a_{33} = c_{py}$, and B is the matrix with $b_{11} = a_{pz}$, $b_{12} = b_{pz}$, $b_{13} = c_{pz}$, $b_{21} = a_{px}$, $b_{22} = b_{px}$, $b_{23} = c_{px}$, $b_{31} = a_{py}$, $b_{32} = b_{py}$, $b_{33} = c_{py}$; thus $AB = 1$, hence $B = A^{-1}$. Note also that $B = A^T$, where T indicates transpose, i.e., $(A^T)_{ij} = a_{ji}$.

The detection point vector $\vec{r} = r\vec{n}$ has components (z, x, y) in ZXY which are independent of (θ_p, ϕ_p) while (u, v, w) in the PQR system depend on (θ_p, ϕ_p) as

$$\vec{r} = z\vec{k} + x\vec{i} + y\vec{j} = u\vec{a}_p + v\vec{b}_p + w\vec{c}_p \quad (30)$$

with $r = \sqrt{(z^2 + x^2 + y^2)} = \sqrt{(u^2 + v^2 + w^2)}$. The matrix relations between the column vectors $u = (u, v, w)^T$ and $z = (z, x, y)^T$ are $u = Az$ and $z = Bu$.

Finally, the photon direction unit vector \vec{a} , defined by the Cherenkov polar and azimuthal angles (θ, ϕ) in PQR, has its emission components $(a_e = \cos\theta, b_e = \sin\theta\cos\phi, c_e = \sin\theta\sin\phi)$ independent of (θ_p, ϕ_p) , while its ZXY components (a_z, a_x, a_y) depend on (θ_p, ϕ_p) as

$$\vec{a} = a_e \vec{a}_p + b_e \vec{b}_p + c_e \vec{c}_p = a_z \vec{k} + a_x \vec{i} + a_y \vec{j} \quad (31)$$

The matrix relations between the column vectors $a = (a_z, a_x, a_y)^T$ and $a_e = (a_e, b_e, c_e)^T$ are $a_e = Aa$ and $a = Ba_e$ with $a^2 = a_e^2 = 1$.

Because the emitted photon plane (containing \vec{n}_e and \vec{a}) also contains C and because the mirror normal (at the reflection point) is in this same plane, therefore the reflected photon will also be in this plane. This is expressed by the vector equation

$$\vec{n} = \mu \vec{n}_e + \nu \vec{a} \quad (32)$$

with μ and ν to be determined. We define the angles (Ω , Ω_e , Ω'), shown in Fig. A1, by the dot products:

$$\begin{aligned}\bar{n} \cdot \bar{n}_e &= \cos\Omega; \\ \bar{a} \cdot \bar{n}_e &= \cos\Omega_e; \\ \bar{a} \cdot \bar{n} &= \cos\Omega'.\end{aligned}$$

Taking the dot product of Eq. (32) with each of ($\bar{a}, \bar{n}_e, \bar{n}$) and solving the first two resultant equations for μ and ν gives

$$\begin{aligned}\mu &= \frac{\sin\Omega'}{\sin\Omega_e}, \\ \nu &= \frac{\sin\Omega}{\sin\Omega_e}.\end{aligned}\tag{33}$$

The third equation is satisfied if $\Omega' = \Omega_e - \Omega$; however, this is always true since the three vectors form a closed triangle. Note that Ω is found directly from experiment as the dot product of the emission point and detection point unit vectors, i.e.,

$$\cos\Omega = \bar{n} \cdot \bar{n}_e = \frac{zz_e + xx_e + yy_e}{rr_e};\tag{34}$$

thus, Ω does not depend on (θ_p, ϕ_p) because both (z, x, y) and (z_e, x_e, y_e) are measured in ZXY. From the geometry of Fig. A1, we find $\Omega = \Omega_e + \Lambda - 2\theta_m$ which, with the sine law relations $r_e \sin\Omega_e = r_m \sin\theta_m = r \sin\Lambda$, becomes

$$\Omega = \Omega_e + \arcsin\left(\frac{r_e \sin\Omega_e}{r}\right) - 2 \arcsin\left(\frac{r_e \sin\Omega_e}{r_m}\right).\tag{35}$$

Thus, we obtain Ω_e (and $\Omega' = \Omega_e - \Omega$) from Ω by numerical inversion of Eq. (35) and find μ and ν from Eq. (33).

An equivalent and computationally faster way of obtaining Ω_e has been recently developed [17]. Consider the two triangles of Fig. A1 containing the $\Omega_a = \Omega_e - \theta_m$ and $\Omega_b = \Lambda - \theta_m$. Straightforward geometry allows us to obtain a quartic equation in $s \equiv \sin\Omega_a$, i.e.,

$$s^4 + a_3 s^3 + a_2 s^2 + a_1 s + a_0 = 0,\tag{36}$$

where $a_3 = -2\eta \sin\Omega$, $a_2 = \eta(a\eta - 2\rho)$, $a_1 = \eta(2\eta - \rho \cos\Omega)$, and $a_0 = (1 - 4\rho^2 \eta^2)/4$ with $\eta \equiv r_m/2r$, $\rho \equiv r/r_e$, and $a \equiv 1 + \rho^2 + 2\rho \cos\Omega$. Solution of the quartic equation gives two real and two complex roots. Of the two real roots, we choose the root which has a mirror hit point $z_m > 0$. The other real root has $z_m < 0$ corresponding to a light ray reflected from the spherical mirror surface upstream of C (where, in fact, no mirror physically exists). From the two triangles, we find the additional relations

$$\begin{aligned}\tan\theta_m &= \frac{s}{2\eta\rho - c}, \\ \Omega_e &= \Omega_a + \theta_m, \\ \tan\Omega_e &= \frac{s}{c - \frac{1}{2\eta\rho}}.\end{aligned}\tag{37}$$

where $c \equiv \cos\Omega_a$. Equations (36) and (37) are equivalent to Eq. (35) but are computationally faster.

We then proceed to solve Eq. (31) for \bar{a} as

$$\bar{a} = \left(\frac{1}{v}\right)\bar{n} - \left(\frac{\mu}{v}\right)\bar{n}_e = \left(\frac{\sin\Omega_e}{\sin\Omega}\right)\bar{n} - \left[\frac{\sin(\Omega_e - \Omega)}{\sin\Omega}\right]\bar{n}_e. \quad (38)$$

Since the components of \bar{a} along $(\bar{a}_p, \bar{b}_p, \bar{c}_p)$ are ($a_e = \cos\theta$, $b_e = \sin\theta\cos\phi$, and $c_e = \sin\theta\sin\phi$), we find for the Cherenkov emission angles (θ, ϕ) , the explicit relations

$$\begin{aligned} \cos\theta &= \left(\frac{\sin\Omega_e}{\sin\Omega}\right)\left(\frac{u}{r}\right) - \left[\frac{\sin(\Omega_e - \Omega)}{\sin\Omega}\right]\left(\frac{u_e}{r_e}\right), \\ \sin\theta\cos\phi &= \left(\frac{\sin\Omega_e}{\sin\Omega}\right)\left(\frac{v}{r}\right) - \left[\frac{\sin(\Omega_e - \Omega)}{\sin\Omega}\right]\left(\frac{v_e}{r_e}\right), \\ \sin\theta\sin\phi &= \left(\frac{\sin\Omega_e}{\sin\Omega}\right)\left(\frac{w}{r}\right) - \left[\frac{\sin(\Omega_e - \Omega)}{\sin\Omega}\right]\left(\frac{w_e}{r_e}\right). \end{aligned} \quad (39)$$

Thus, θ and ϕ are obtained from (Ω, Ω_e) , (u_e, v_e, w_e) , and (u, v, w) . The (θ_p, ϕ_p) dependence enters through (u_e, v_e, w_e) and (u, v, w) , i.e., via the matrix A of Eq. (28). This reconstruction is quite general (it works for any detector surface, e.g., flat) and removes all but intrinsic aberrations of the image.

Clearly, the solution for Ω_e (and Λ and θ_m) is independent of (θ_p, ϕ_p) , since physically, it represents a light ray propagating from \bar{r}_e to \bar{r} . Similarly, the timing equation (Sec. 3.4) is also independent of (θ_p, ϕ_p) .

This completes the summary of the Cherenkov angle reconstruction method [7].

3.3 Approximate Determination of Particle Direction

The geometry of the LBL-RICH makes it difficult (or impossible) to implement a tracker inside the water volume; however, (θ_p, ϕ_p) can be found in good approximation from the center of the ring image. Since the ring images can be identified (see Figs. 7-14), we assume that an array of image points (z_i, x_i, y_i) and arrival times t_i are known ($i = 1$ to N). From these points, we can approximately determine the particle direction (even if \bar{r}_e is not known) by assuming that the array (z_i, x_i, y_i) satisfies the equation of a circle on a sphere. Intersection of a cone (cone angle θ , cone direction θ_p, ϕ_p) with a sphere of radius r gives the equation of a circle on a sphere as

$$\begin{aligned} z_i + \xi x_i + \psi y_i - \lambda r &= 0, \\ \xi &= \tan\theta_p \cos\phi_p, \\ \psi &= \tan\theta_p \sin\phi_p, \\ \lambda &= \cos\theta/\cos\theta_p. \end{aligned} \quad (40)$$

Minimizing the function $\chi^2 = \sum_1^N (z_i + \xi x_i + \psi y_i - \lambda r)^2$ with respect to the unknown coefficients (ξ, ψ, λ) leads to the equations

$$\begin{aligned}\xi &= \frac{\sigma_{xy}\sigma_{yz} - \sigma_{xz}\sigma_{yy}}{\sigma_{xx}\sigma_{yy} - \sigma_{xy}\sigma_{xy}}, \\ \psi &= \frac{\sigma_{xy}\sigma_{xz} - \sigma_{yz}\sigma_{xx}}{\sigma_{xx}\sigma_{yy} - \sigma_{xy}\sigma_{xy}}, \\ \lambda r &= \langle z \rangle + \xi \langle x \rangle + \psi \langle y \rangle.\end{aligned}\quad (41)$$

where $\langle x \rangle = \frac{1}{N} \sum x_i$, etc., $\langle xy \rangle = \frac{1}{N} \sum x_i y_i$, etc., $\sigma_{xy} = \langle xy \rangle - \langle x \rangle \langle y \rangle$, etc.

Thus,

$$\begin{aligned}\cos \theta_p &= \frac{1}{\sqrt{1 + \xi^2 + \psi^2}}, \\ \cos \phi_p &= \frac{\xi}{\sqrt{\xi^2 + \psi^2}}, \\ \sin \phi_p &= \frac{\psi}{\sqrt{\xi^2 + \psi^2}}, \\ \cos \theta &= \frac{\langle z \rangle + \xi \langle x \rangle + \psi \langle y \rangle}{r \sqrt{1 + \xi^2 + \psi^2}}.\end{aligned}\quad (42)$$

This zero impact parameter ($u_e = v_e = 0$), spherical detector surface approximation provides an initial estimate of (θ_p, ϕ_p) but not of θ ; however, this is not a problem because the reconstruction algorithm [Eq. (39)] gives a precise estimate for (θ, ϕ) .

3.4 Timing Measurements and Determination of the Track Parameters

The track parameters z_e , x_e , and y_e can be determined from the measurement of time. The ring image pattern defines an array (z_i, x_i, y_i) of image points ($i = 1$ to N) and an associated photon arrival time $t_i \pm \sigma_t$ at the PM. The photon pathlengths are ℓ_1 from the emission point \bar{r}_e to the mirror hit point \bar{r}_m , and ℓ_2 from \bar{r}_m to the photon detection point \bar{r} . These are found from Fig. A1, using the sine law relations $r_e \sin \Omega_e = r_m \sin \theta_m = r \sin \Lambda \equiv r_a$, as

$$\begin{aligned}\ell_1 &= r_m \cos \theta_m - r_e \cos \Omega_e, \\ \ell_2 &= r_m \cos \theta_m - r \cos \Lambda.\end{aligned}\quad (43)$$

The total pathlength $\ell = \ell_1 + \ell_2$ is obtained from the detection point $r = \sqrt{(z^2 + x^2 + y^2)}$ and the assumed emission point $r_e = \sqrt{(z_e^2 + x_e^2 + y_e^2)}$ as

$$\ell = \ell_1 + \ell_2 = \frac{ct}{n} = 2\sqrt{r_m^2 - r_e^2 + r_b^2} - \sqrt{r^2 - r_e^2 + r_b^2} - r_b, \quad (44)$$

where Ω_e is from Eq. (35) [or Eqs. (36) and (37)], $r_b \equiv r_e \cos \Omega_e$, and $t = n\ell/c$ is the time from photon emission to detection. As expected, Eq. (44) is independent of particle direction (θ_p, ϕ_p) .

3.5 Reconstruction of (θ, ϕ) and Determination of Track Parameters $(z_e, x_e, y_e, \theta_p, \phi_p)$

The reconstruction and track finding strategy can now be stated:

- (1) an image is visually identified with measured hit points and time (z_i, x_i, y_i, t_i) ;
- (2) the initial emission point and emission time (z_e, x_e, y_e, t_e) are chosen randomly in the water volume and during the beam spill;
- (3) Ω is calculated from Eq. (34);
- (4) Ω_e is determined by numerically inverting Eq. (35) or solving Eqs. (36) and (37);
- (5) an initial estimate of particle direction (θ_p, ϕ_p) is found from Eq. (42);
- (6) values for (θ, ϕ) are then determined from Eq. (39) using Eqs. (28) and (29);
- (7) the time-detector $\chi^2 = \chi_{td}^2$ function is constructed from measured t_i and t_i^{th} from Eq. (44) as

$$\chi_{td}^2 = \sum_1^N \left(\frac{t_i - t_i^{th}}{\sigma_t} \right)^2 \quad (45)$$

and minimized by varying (z_e, x_e, y_e, t_e) . Since absolute time of the primary interaction cannot be determined (or known from

the beam spill because 20 beam bunches will be inside the water radiator at any given time), the emission time t_e may be determined from the ring. However, because χ_{td}^2 depends only on time differences, these can be referenced to any convenient zero which in our case is the onset of the SPS beam spill cycle. We have shown for the geometry of Fig. 1 with 1 ns time bins, 125 mm x, y pixels (and with 1λ emission point variation, chromatic, multiple scattering, and energy loss aberrations) that the χ_{td}^2 function near its minimum varies by about a factor of two for variations of 100 mm of the average emission point. The problem of finding a good starting point (z_e, x_e, y_e, t_e) within the large radiator volume is considered in Sec. 4.

- (8) A finer determination of the track parameters $(z_e, x_e, y_e, \theta_p, \phi_p)$ and (θ, ϕ) is obtained by minimizing the width of the θ distribution, i.e.,

$$\sigma_\theta^2 = \frac{1}{N} \sum_1^N \theta_i^2 - \left(\frac{1}{N} \sum_1^N \theta_i \right)^2, \quad (46)$$

by varying the track parameters near the minimum of the χ_{td}^2 function [Eq. (45)].

3.6 Vertex Point Determination

The distance along the track from vertex to emission point u_{ve} varies from photon to photon with $\langle u_{ve} \rangle = \lambda/2 = 425$ mm for the average hadron. A better estimate is obtained from the number of imaged points N , i.e.,

$$u_{ve} = \frac{N}{\varepsilon_g \varepsilon_a N_0 \sin^2 \theta} \quad (47)$$

corrected for geometrical efficiency ε_g , i.e., the fraction of photons which hit the mirror and are imaged (without hitting the side walls). This is obtained by simulation from the assumed emission point (z_e, x_e, y_e) . In this simulation, (θ_p, ϕ_p) and θ are needed and ϕ is varied to find the efficiency. The absorption term $\varepsilon_a = e^{-\mu \ell}$ is evaluated from ℓ [Eq. (44)] using the measured water absorption coefficient $\mu = \mu(E)$ (Ref. [15]).

If two ring images (1 and 2) are fit by the preceding algorithm (Sec. 3.4) and if their emission points \bar{r}_{e1} and \bar{r}_{e2} are near each other (i.e., $\Delta r_{12} = |\bar{r}_{e1} - \bar{r}_{e2}| \approx \lambda$), then they are candidates to have a common vertex. The vector equation for the vertex point is

$$\bar{r}_v = u_{va1} \bar{a}_{p1} + v_{e1} \bar{b}_{p1} + w_{e1} \bar{c}_{p1} = u_{va2} \bar{a}_{p2} + v_{e2} \bar{b}_{p2} + w_{e2} \bar{c}_{p2}, \quad (48)$$

where $u_{va1} = u_{e1} \pm u_{ve1}$ and $u_{va2} = u_{e2} \pm u_{ve2}$ [u_{ve1} and u_{ve2} are found from Eq. (47)]. Both signs are negative for a primary vertex, whereas one sign is negative and the other positive for a scatter or decay vertex. The three components of Eq. (48) used in a χ^2 minimization will strongly limit the vertex point with $C = 3M$ constraints (M is the number of charged vertex tracks). Thus, even a two track vertex will provide six equations on the vertex point. We estimate that the vertex point can be found with cm-like accuracy although this has not yet been verified by simulation.

4. Photon Detection with PM's at the Mirror Surface

It is essential to find the photon emission point four-vector (\bar{r}_e, t_e) in order that the Cherenkov angle reconstruction can be implemented (step 2 of Sec. 3.5). We have shown that random start points converge to the correct minimum if the point is within a 3 m radius four sphere about the true emission point. To explore the space inside a $(30 \text{ m})^3$ volume would require choosing 10^3 random start points. In the time coordinate, the radiator is 1350 m long (i.e., a 6 μs beam spill with $c/n = 0.225 \text{ m/ns}$), hence 450 segments of ± 1.5 m length. Combining these 450 points with the 1000 volume start points implies about 450 k random start points, which appear excessive.

For this reason, we have investigated the effect of replacing 4% of the reflecting mirror surface area, i.e., 36 m^2 with 2880 PM's of 127 mm diameter so as to directly detect Cherenkov photons (a la IMB,

Kamiokande, and Super-Kamiokande). This will result in a substantial sample of mirror PM (mPM) hits, since the mPM cover is 1/5 of the detector PM (dPM) cover, and thus, provides 160 mPM hits compared with 800 dPM hits.

4.1 Determination of the Photon Emission Point and Time

We use a four-vector formulation of the problem due to G. Fiorentini [18] and denote by $\xi_\alpha \equiv (\bar{r}, ct/n)$ the four-vector components of the i th, mPM hit (subscripts i and m are dropped). Denoting the emission point vector components $\psi_\alpha \equiv (\bar{r}_e, ct_e/n)$, then the equation for the photon vector components is just the difference between hit and emission points, i.e., $a_\alpha = \xi_\alpha - \psi_\alpha$. We define the coordinate vector $\eta_\alpha \equiv \xi_\alpha - \langle \xi_\alpha \rangle$ so that its average over the i hits is zero (i.e., $\langle \eta_\alpha \rangle = 0$) and the vector $\delta_\alpha \equiv \psi_\alpha - \langle \xi_\alpha \rangle$, thus $a_\alpha = \eta_\alpha - \delta_\alpha$. The condition for a_α to be a photon four vector is then

$$a_\alpha a_\alpha = (\eta_\alpha - \delta_\alpha)^2 = \eta_\alpha \eta_\alpha - 2\eta_\alpha \delta_\alpha + \delta_\alpha \delta_\alpha = 0; \quad (49)$$

averaging over the i photon hits and recalling that $\langle \eta_\alpha \rangle = 0$ gives

$$\begin{aligned} \langle \eta_\alpha \eta_\alpha \rangle &\equiv \langle s^2 \rangle = -\delta_\alpha \delta_\alpha \equiv -s_e^2; \\ \langle s^2 \rangle &= \langle z^2 \rangle + \langle x^2 \rangle + \langle y^2 \rangle - \langle t^2 \rangle; \\ s_e^2 &= z_e^2 + x_e^2 + y_e^2 - t_e^2, \end{aligned} \quad (50)$$

where (z, x, y, t) are the hit mPM coordinates with time converted to space by the velocity factor c/n . Equation (50) thus gives a quadratic constraint on the unknowns (z_e, x_e, y_e, t_e) in the form $s_e^2 = -\langle s^2 \rangle$, i.e., as averages over known mirror hit points $\langle s^2 \rangle$. This relation constrains but does not determine (z_e, x_e, y_e, t_e) . For this purpose, we multiply Eq. (50) by η_β and again average over hit points to obtain

$$\begin{aligned} \langle \eta^2 \eta_\beta \rangle - 2\delta_\alpha \langle \eta_\alpha \eta_\beta \rangle &= 0; \\ \delta_\alpha T_{\alpha\beta} &= V_\beta; \\ T_{\alpha\beta} &= \langle \eta_\alpha \eta_\beta \rangle; \\ V_\beta &= \langle \eta^2 \eta_\beta \rangle / 2, \end{aligned} \quad (51)$$

where the third term of Eq. (49) drops out because $\langle \eta_\beta \rangle = 0$. This gives a set of four linear equations for $\delta_\alpha = (z_e, x_e, y_e, t_e)$ in terms of the tensor $T_{\alpha\beta}$ and the vector V_β . These are respectively, quadratic and cubic moments averaged over hit points, i.e., $T_{11} = \langle z^2 \rangle$, $T_{12} = \langle zx \rangle$, $T_{13} = \langle zy \rangle$, $T_{14} = -\langle zt \rangle$, $T_{21} = \langle zx \rangle$, $T_{22} = \langle x^2 \rangle$, $T_{23} = \langle xy \rangle$, $T_{24} = -\langle xt \rangle$, $T_{31} = \langle zy \rangle$, $T_{32} = \langle xy \rangle$, $T_{33} = \langle y^2 \rangle$, $T_{34} = -\langle yt \rangle$, $T_{41} = \langle zt \rangle$, $T_{42} = \langle xt \rangle$, $T_{43} = \langle yt \rangle$, $T_{44} = -\langle t^2 \rangle$, and $2V_1 = \langle zs^2 \rangle = \langle z^3 \rangle + \langle zx^2 \rangle + \langle zy^2 \rangle - \langle zt^2 \rangle$, $2V_2 = \langle xs^2 \rangle$, $2V_3 = \langle ys^2 \rangle$, $2V_4 = \langle ts^2 \rangle$. In order to obtain stable and accurate (meaningful) solutions to these linear equations, it was necessary to use the method of Gaussian elimination with partial pivoting [19].

Unfortunately, the constraint [Eq. (50)] is not contained in the linear relations for δ_α of Eq. (51). We have simulated many random events with full errors and aberrations and plotted the distance between the

solution values $(z_{es}, x_{es}, y_{es}, t_{es})$ to input values (z_e, x_e, y_e, t_e) in the form of the four-radius $r_4 = \sqrt{[(z_{es}-z_e)^2+(x_{es}-x_e)^2+(y_{es}-y_e)^2+(t_{es}-t_e)^2]}$ versus $C = [s_e^2+\langle s^2 \rangle]/\langle s^2 \rangle$, the normalized constraint. It was found that for $-1 < C < 1$, the four radius is within 3 m of the true emission point; hence, it is sufficient to guarantee that the χ^2 algorithm of Sec. 3.4 converges to the correct minima. Moreover, we found that about 90% of the random events have $|C| \leq 1$.

The above results may be compared to the standard χ^2 formulation of the problem. Since the i th hit point is caused by a photon, it obeys the spherical wave relation

$$f_i = (z_i - z_e)^2 + (x_i - x_e)^2 + (y_i - y_e)^2 - (t_i - t_e)^2 = 0. \quad (52)$$

Averaging over the i hits gives

$$\langle f \rangle = \langle z \rangle^2 + \langle x \rangle^2 + \langle y \rangle^2 - \langle t \rangle^2 + z_e^2 + x_e^2 + y_e^2 - t_e^2 = \langle s \rangle^2 + s_e^2 = 0; \quad (53)$$

thus, we recover the constraint of Eq. (50). Here we have used, as before, the hit points with their average subtracted so that $\langle z \rangle = \langle x \rangle = \langle y \rangle = \langle t \rangle = 0$. We now define the spherical wave to mirror χ^2 as

$$\chi_{swm}^2 = \sum_i^N \left(\frac{f_i}{\sigma_{f_i}} \right)^2, \quad (54)$$

$$\sigma_{f_i} = 2\sqrt{(z_i - z_e)^2 \sigma_z^2 + (x_i - x_e)^2 \sigma_x^2 + (y_i - y_e)^2 \sigma_y^2 + (t_i - t_e)^2 \sigma_t^2}.$$

Requiring $\partial\chi^2/\partial z_e = 0$, $\partial\chi^2/\partial x_e = 0$, $\partial\chi^2/\partial y_e = 0$, $\partial\chi^2/\partial t_e = 0$ results in the same formulas as Eq. (51) except the diagonal elements T_{ii} have the additional term ϵ , i.e., $T_{11} = \langle z^2 \rangle + \epsilon$, $T_{22} = \langle x^2 \rangle + \epsilon$, $T_{33} = \langle y^2 \rangle + \epsilon$, $T_{44} = -\langle t^2 \rangle + \epsilon$ (where $2\epsilon = C\langle s^2 \rangle = \langle s^2 \rangle + z_e^2 + x_e^2 + y_e^2 - t_e^2$); thus the equations are no longer linear (i.e., cubic) in $(z_e, x_e, y_e, \text{ and } t_e)$ unless the constraint $C = 0$ is satisfied. An attempt to find an iterative solution (the diagonal elements were increased by the ϵ found in the preceding iteration) failed since the solution did not converge. Possibly, this constraint may be imposed by the method of Lagrangian multipliers. In general, and for any start point, the χ_{swm}^2 function must be minimized to find the best emission point vector $(z_e, x_e, y_e, \text{ and } t_e)$.

4.2 Determination of the Particle Direction

An approximate algorithm to determine particle direction using dPM hits has already been given in Sec. 3.3, but a more precise algorithm using mPM hits would be advantageous for choosing a better start point for the χ^2 minimizations (Step 2 of Sec. 3.5).

We present here an algorithm due to G. Fiorentini [19] using again the notation of the preceding section. The three-vector η_i represents the k th mirror hit point (average subtracted, subscripts k and m dropped), thus the average over the k hits $\langle \eta_i \rangle = 0$. The emission point vector in the same coordinate system is δ_i , hence the photon vector (of

length ρ) is $\rho_i = \rho a_i = \eta_i - \delta_i$ and its dot product with particle direction is $\rho a_i a_{pi} = \rho \cos\theta = (\eta_i - \delta_i) a_{pi}$. The length ρ is simply the time difference $\eta_4 - \delta_4$, and hence the basic equation is $(\eta_i - \delta_i) s_i = (\eta_4 - \delta_4)$ in the variables $s_i = a_{pi} / \cos\theta$. Averaging over hits gives the constraint $\delta_i s_i = \delta_4$. Multiplying the basic equation by η_m and averaging gives a set of linear equations $T_{mi} s_i = V_m$, where the tensor $T_{mi} = \langle \eta_m \eta_i \rangle$ and the vector $V_m = \langle \eta_m \eta_4 \rangle$. Expressed in terms of the hit points (z, x, y, t) , we get the same tensor as given in Sec. 4.1 (i.e., $T_{11} = \langle z^2 \rangle$, $T_{12} = \langle zx \rangle$, ...) whereas the vector components are $V_1 = \langle tz \rangle$, $V_2 = \langle tx \rangle$, $V_3 = \langle ty \rangle$. Note that the three solutions s_i just suffice to determine θ , θ_p , and ϕ_p . Written out in full, the constraint has the form $z_e s_1 + x_e s_2 + y_e s_3 = t_e$ where (z_e, x_e, y_e, t_e) are found from Eq. (51).

The problem then is to solve a set of three linear equations with a linear constraint. The solution of the linear equations by Gaussian elimination with partial pivoting [19] is straightforward, but we have not yet been able to include the constraint. The solutions with emission point, pixel, and timing errors included are excellent if the hit (data) points are generated without chromatic aberrations, multiple scattering, or energy loss; however, once these are included, the solutions become unstable and useless. For this reason, we looked for another less elegant algorithm which can provide some sensitivity to particle direction from mirror hit points.

The vector equation of the photon hit point $\vec{r} = \vec{r}_e + \rho \vec{a}$, where again ρ is the distance between the emission and hit points, and \vec{a} the photon direction unit vector [Eq. (31)]. In the PQR coordinate system,

the components are $u_i - u_{ei} = \rho_i \cos\theta$, $v_i - v_e = \rho_i \sin\theta \cos\phi$, and $w_i - w_e = \rho_i \sin\theta \sin\phi$ where ρ_i is the distance between i th emission and hit points. Recall that impact parameter coordinates (v_e and w_e) do not depend on i because they are constant anywhere along the track, whereas u_e varies with the point of emission along the track. Eliminating ρ_i and ϕ , we obtain the equation of a cone $g_i = 0$ and then solve for u_{ei} , i.e.,

$$g_i = (v_i - v_e)^2 + (w_i - w_e)^2 - \tan^2\theta (u_i - u_{ei})^2 = 0, \quad (55)$$

$$u_{ei} = u_i - \frac{\sqrt{[(v_i - v_e)^2 + (w_i - w_e)^2]}}{\tan\theta}.$$

The emission point u_{ei} along the track is determined if θ , θ_p , ϕ_p are assumed and the impact parameters v_e and w_e are known. For this purpose, we use the solution of Eq. (51) which gives (z_e, x_e, y_e, t_e) from the mirror hit points (z_i, x_i, y_i, t_i) . The assumed (θ_p, ϕ_p) direction defines the matrices A and B; thus $u_e = A z_e$ can be calculated and impact parameters v_e and w_e extracted. Since these are constant along the track, we use these in Eq. (55) along with the transformed hit point $u_i = A z_i$ to find the column vector $u_{ei} = (u_{ei}, v_e, w_e)^T$. Transforming back via $z_{ei} = B u_{ei}$ gives a column vector (z_{ei}, x_{ei}, y_{ei}) for each hit point which inserted into Eq. (52) gives the cone-spherical wave-mirror (cswm) direction dependent constraint

$$\chi_{\text{cswm}}^2 = \sum_i^N \left(\frac{g_i}{\sigma_{g_i}} \right)^2,$$

$$\sigma_{g_i} = 2 \sqrt{(Z\sigma_z)^2 + (X\sigma_x)^2 + (Y\sigma_y)^2},$$

$$Z = (v - v_e)b_{pz} + (w - w_e)c_{pz} - \tan^2 \theta (u - u_{ei})a_{pz}, \quad (56)$$

$$X = (v - v_e)b_{px} + (w - w_e)c_{px} - \tan^2 \theta (u - u_{ei})a_{px},$$

$$Y = (v - v_e)b_{py} + (w - w_e)c_{py} - \tan^2 \theta (u - u_{ei})a_{py}.$$

In summary, we now have three χ^2 functions to minimize χ_{td}^2 [Eq. (45)] and χ_{swm}^2 [Eq. (54)], which depend only on the emission point vector and the χ_{cswm}^2 function [Eq. (56)] which depends both on emission point and particle direction (θ_p, ϕ_p). In addition, the width σ_θ of the reconstructed Cherenkov angle [Eq. (46)] depends both on emission point and particle direction.

We calculated the values of $\chi_{td}^2, \chi_{\text{swm}}^2, \chi_{\text{cswm}}^2, \theta$, and σ_θ vs $\Delta(t_e, z_e, x_e, y_e, \theta, \theta_p, \phi_p)$ for representative events with realistic errors (Δ here indicates the difference between the true value of the variable and its assumed value). Each event was generated at a random point and time in the water volume (z_e, x_e, y_e, t_e) with a random direction (θ_p, ϕ_p), random pathlength (ℓ), and an emission point random between ($0 < u_e < \ell$). The ring images included chromatic aberrations, multiple scattering, and energy loss appropriate to the water radiating medium. The results showed that track variables (t_e, z_e, x_e, y_e) were determined to about 100 mm while the particle direction (θ_p, ϕ_p) was found within 5 mrad. More important, the values of θ and σ_θ were found always to

be equal to the generated values thus allowing velocity determination and, in addition, momentum and mass determination over the range of MSD.

5. Beams and Sites

5.1 The CERN-SPS Extracted Beam

The CERN-SPS beam operates at 200 MHz, thus with a 5 ns periodicity. This means that succeeding RF bunches are separated in the water target by only 1.5 m; hence absolute timing cannot determine the interaction vertex point (this would be possible if the RF bunches were separated by > 100 ns). In other words, at any given time within an SPS burst, there will be 20 RF bunches inside the water target.

One, two, or three SPS beam bursts can be extracted every SPS cycle of 14 sec. If one burst is extracted, it will be 23 μs long and contain 1.3×10^{13} p. If two bursts are extracted, they will be 10 μs long separated by 50 ms each with 1.3×10^{13} p giving 2.6×10^{13} p/cycle. If three bursts are extracted, they will be 6 μs long separated by 50 ms, hence 3.9×10^{13} p/cycle. For a 44% SPS duty factor, there will be 10^6 cycles/y and so $\approx 4 \times 10^{19}$ p/y (Ref. [20]).

5.2 Neutrino Beam and Event Rates

The designed broad band neutrino beam ($1 < E_\nu < 20$ GeV) has a flux of 500 events/kt- 10^{19} p; thus for 4×10^{19} p/y, the rate will be 2000 events/kt-y (Ref. [21]). Since the LBL-RICH contains 22.5 fiducial kt of water, it should amass up to 45 k events/y (for no oscillations, i.e., $\Delta m^2 = 0$).

5.3 Where to Site the LBL-RICH

5.3.1 Outside the Gran Sasso Tunnel

As is clear from Fig. 1, the Gran Sasso tunnel would have to be 43 m in diameter to contain a $(30 \text{ m})^3$ cube. This is twice the diameter of the present and future Gran Sasso tunnels, so we have investigated operation of the LBL-RICH above ground. The possibility is to use an existing Gran Sasso tunnel of about 19 m diameter, but extending the length of the radiator to 100 m will be considered in the next section.

We assume the full unshielded cosmic ray flux of $180/\text{m}^2\text{-s}$ (Ref. [22]). For the 900 m^2 surface area of LBL-RICH, the rate will be 0.16 MHz; thus, during a beam burst of $6 \mu\text{s}$, we expect one muon to traverse the LBL-RICH. Since 3×10^6 SPS bursts result in 45 k events, the specific event rate is 0.015 events/burst or one signal event (S) per

67 bursts. During this particular burst, we expect one background muon (B), thus $S/B \approx 1$. The other 66 bursts will contain only an obvious B event which cannot be confused with S because it lies in another burst. At least four methods are available to reduce B to a negligible level. They are:

- (1) By optically shielding the PM's so they only view the mirrors.
- (2) By timing. Recall that the PM hits are binned in buckets of 1 ns width over a period of 128 ns. The B event will arrive randomly over the $6 \mu\text{s}$ burst gate since, because of its directionality, it cannot initiate the 100 PM trigger. The true S event arrives (during the $6 \mu\text{s}$ burst) with ≤ 128 ns dispersion relative to the 100 PM trigger signal, thus allowing a B reduction factor of $6000/128 = 47$.
- (3) By pattern. Since the B events are mostly vertical, they do not form good images, whereas the S events are mostly longitudinal and do form good images.
- (4) By massive shielding. Even though the LBL-RICH will be above ground, it should be placed behind a mountain (when viewed from CERN), thus screening out the more horizontal muon tracks.

The cost estimate with mHPD's and dHPD's is 25 MSF.

5.3.2 Inside a Gran Sasso Tunnel

A possible layout of the LBL-RICH inside a Gran Sasso tunnel of 19 m diameter is shown in Fig. 15. Using five sections of 20 m length and 18.6 m diameter, we can obtain the same 27 kt water mass. The HPD image plane is located at 11.5 m from the mirror's center of curvature, and the image radius is about 8.4 m.

This solution has several advantages; namely, it is shielded both from cosmic rays and from ecologists. Another advantage is that the muons will be extremely well measured in several of the five sections. The device becomes a Cherenkov total energy calorimeter with $1000 \text{ pe/m} = 625 \text{ pe/GeV}$.

The disadvantages are that it has a smaller electron shower fiducial mass since the last 5 m of each section is needed to contain the shower (20 kt compared to 22.5 kt) and requires more HPD surface area [1360 compared to 900 m^2 , thus $5 \times 1100 = 5500$ HPD's of 250 mm in diameter compared to 3600 for the $(30 \text{ m})^3$ radiator].

The total cost estimate here is 40.6 MSF compared to the outside option of 25 MSF; hence costs scale for the same water mass approximately as the inverse ratio of mirror focal length (i.e., $30/20 = 1.5$, whereas the inside option is actually 1.62 times more expensive).

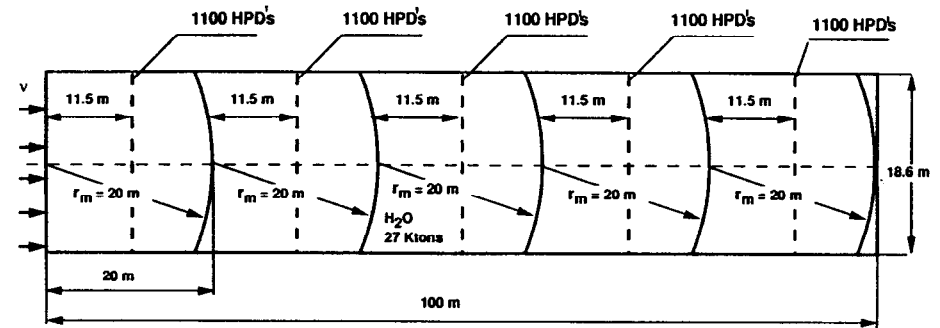


Fig. 15. The layout of the 27 kt water target and radiator filling a Gran Sasso tunnel of 18.6 m diameter. Five equivalent sections of 20 m length have reflecting mirrors of 20 m curvature placed at the end of each section. The detector HPD plane array (20% coverage) is placed 11.5 m downstream from the mirror center of curvature.

6. The LBL-RICH Physics Reach

The maximal mixing model of Harrison *et al.* [23] (which fits all existing neutrino data) predicts a large muon disappearance effect (44%) and a large electron appearance effect (22%) in the region $50 < L/E_\nu < 700$, thus for $1 < E_\nu < 15$ at $L = 732$ km. This region is easily accessible with the broad band beam in the LBL-RICH. The muon rate will be large without (and measurably less with) oscillations, whereas the electron rate will be small without (and measurably more with) oscillations. Since the LBL-RICH has good energy resolution for muons, electrons, and hadrons, it can fine-bin the muon or electron type events vs L/E_ν so as to observe the maximum oscillation swings.

In the two-neutrino mixing analysis, we expect to reach $\Delta m^2 \approx 9.2 \times 10^{-4} \text{ eV}^2/\sin(2\theta)$ for $\nu_\mu \rightarrow \nu_\tau$ oscillations via the reaction $\nu_\tau + n \rightarrow \tau + p$ with decay $\tau \rightarrow e + \nu_e + \nu_\tau$ by cuts on p_τ and E_e . Neutrino interactions in this low-energy, wide-band beam ($1 < E_\nu < 20$ GeV) are $\approx 95\%$ deep inelastic (DIS) (67% CC, 33% NC) and $\approx 5\%$ quasi-elastic (QEL). The beam flux is 2000 events/kt-y, hence the LBL-RICH (22.5 kt fiducial) will detect 2.3×10^5 events in five years. The number of ν_μ quasi-elastic events is $N_\mu(\text{QEL}) \approx 1.2 \times 10^4$ with a ν_e quasi-elastic background of $N_e(\text{QEL}) \approx 60$ (since $\nu_e/\nu_\mu = 0.5\%$) but is reduced to 0.4 by the kinematical cuts (6×10^{-3}) (Ref. [24]). The number of NC-DIS events is much larger (7.7×10^4) but drops to 15 by the same kinematical cuts (2×10^{-4}) (Ref. [24]). Further purification must be obtained from the ring patterns. If no $\tau \rightarrow e$ candidates are observed in this event sample

($N_{\tau e} = 2.3$ at the 90% confidence level), we obtain the oscillation probability

$$P = \frac{N_{\tau e}}{(N_\mu)(\text{BR})(\text{eff})\left(\frac{\sigma_{\nu\tau}}{\sigma_{\nu\mu}}\right)} = \frac{2.3}{(1.2 \times 10^4)(0.18)(0.21)(0.7)} = 0.0072, \quad (57)$$

where BR is the $\tau \rightarrow e\nu\nu$ branching ratio, eff = signal efficiency = 0.21 (0.23 for p above threshold, 0.9 for $p_\tau > 0.3$ GeV), and 0.7 is the ratio of the ν_τ and ν_μ cross sections. However, for small oscillations, we can write

$$\sqrt{P} = \sin(2\theta) \frac{1.27 \Delta m^2 L}{E_\nu} = 0.085; \quad (58)$$

hence for Gran Sasso at $L = 732$ km and with neutrino beam energy $E_\nu = 10$ GeV, we find

$$\Delta m^2 = \frac{9.2 \times 10^{-4}}{\sin(2\theta)}. \quad (59)$$

7. Summary

We have shown how a RICH counter can measure momentum and have applied this method to investigate long baseline neutrino oscillation experiments. This method allows large mass targets, but with measurement of momentum, direction, velocity, mass, and absolute charge for hadrons and muons. In addition, electrons and gammas can be measured by calorimetry in water with good energy and excellent direction resolution.

References

- [1] J. L. Guyonnet *et al.*, Nucl. Instrum. Methods A **343**, 178 (1994) and J. Séguinot *et al.*, Nucl. Instrum. Methods A **314**, 465 (1992).
- [2] J. Séguinot *et al.*, Nucl. Instrum. Methods A **371**, 64 (1996).
- [3] T. Ypsilantis and J. Séguinot, Nucl. Instrum. Methods A **368**, 229 (1995).
- [4] T. Ypsilantis *et al.*, Nucl. Instrum. Methods A **371**, 330 (1996).
- [5] A. Zichichi, "Perspectives of Underground Physics: The Gran Sasso Project," CERN-EP/88-28.
- [6] Letter of Intent for the Long Baseline RICH submitted on 1/1/96 to Laboratorio Nazionale del Gran Sasso: "A 27 kton Liquid Water Target and RICH Photon Counter to Detect Oscillations in the CERN-Gran Sasso Neutrino Beam," T. Ypsilantis, spokesman.
- [7] T. Ypsilantis and J. Séguinot, Nucl. Instrum. Methods A **343**, 30 (1994).
- [8] D. Hatzifotiadou *et al.*, College de France, LPC/94-29.
- [9] Y. Goldschmidt-Clermont *et al.*, Proc. Phys. Soc. **61**, 138 (1948).
- [10] U. Camerini *et al.*, Phil. Mag. **41**, 413 (1950).
- [11] R. Barlow, *Statistics* (John Wiley and Sons), Sec. 5.2.3.
- [12] R. De Salvo, CLNS 87-92, Cornell University, Ithaca, NY. See also R. De Salvo *et al.*, Nucl. Instrum. Methods A **315**, 375 (1992); Nucl. Instrum. Methods A **365**, 76 (1995).
- [13] E. Chesi *et al.*, Nucl. Instrum. Methods A **387**, 222 (1997).
- [14] R. De Salvo (private communication).
- [15] J. Quickendon *et al.*, J. Chem. Phys. **72**, 4416 (1980).
- [16] I. Thormahlen, J. Straub, and U. Grigull, J. Phys. Chem. Ref. Data **14**, 933 (1985).
- [17] R. Forty, Nucl. Instrum. Methods A **384**, 167 (1996).
- [18] G. Fiorentini (private communication).
- [19] G. E. Forsythe and C. B. Moler, *Computer Solution of Linear Algebraic Systems* (Prentice-Hall Inc.), pp. 68-70.
- [20] E. Weisse (private communication).
- [21] A. Ball *et al.*, Nucl. Instrum. Methods, in press.
- [22] Particle Data Group, Phys. Rev. D **50**, 1173 (1994). See p. 1269.
- [23] P. F. Harrison, D. H. Perkins, and W. G. Scott, Phys. Lett. B **349**, 137 (1995).
- [24] A. Rubbia, Report to the CERN Medium/Long Baseline Working Group (1996).

Appendix A

We consider the more general geometry of a ring image. We define two different coordinate systems as shown in Fig. A1, the ZXY system, fixed relative to the mirror, with unit vectors $(\bar{k}, \bar{i}, \bar{j})$ and the PQR system, fixed to each track and defined from C such that P is parallel to the track and Q and R are normal to the track with unit vectors $(\bar{a}_p, \bar{b}_p, \bar{c}_p)$. The photon emission point is (z_e, x_e, y_e) in the ZXY system and (u_e, v_e, w_e) in the PQR system. The photon detection point is (z, x, y) in the ZXY system and (u, v, w) in the PQR system.

An external particle tracker would directly measure (u_e, v_e, w_e) and the photon detector measures (z, x, y) . The other coordinates (z_e, x_e, y_e) and (u, v, w) must then be determined from knowledge of (θ_p, ϕ_p) via Eqs. (29) and (30).

In the LBL-RICH case, the mirror tracker measures (z_e, x_e, y_e, t_e) and the photon detector (z, x, y) . Thus, (u_e, v_e, w_e) and (u, v, w) are functions of (θ_p, ϕ_p) via Eqs. (28) and (30).

The emission point vector \bar{r}_e , the photon vector \bar{a} , and the mirror hit vector \bar{r}_m define one triangle with included angles $\pi - \Omega_e$, θ_m , and Ω_a as shown in Fig. A1. The mirror hit vector \bar{r}_m with the reflected photon vector \bar{a}_r and the detected point vector \bar{r} define a second triangle with angles θ_m , $\pi - \Lambda$, and Ω_b ; hence since $\Omega = \Omega_a + \Omega_b = \Omega_e + \Lambda - 2\theta_m$ and $r_e \sin \Omega_e = r_m \sin \theta_m = r \sin \Lambda (\equiv r_a)$, then Eq. (35) is proven.

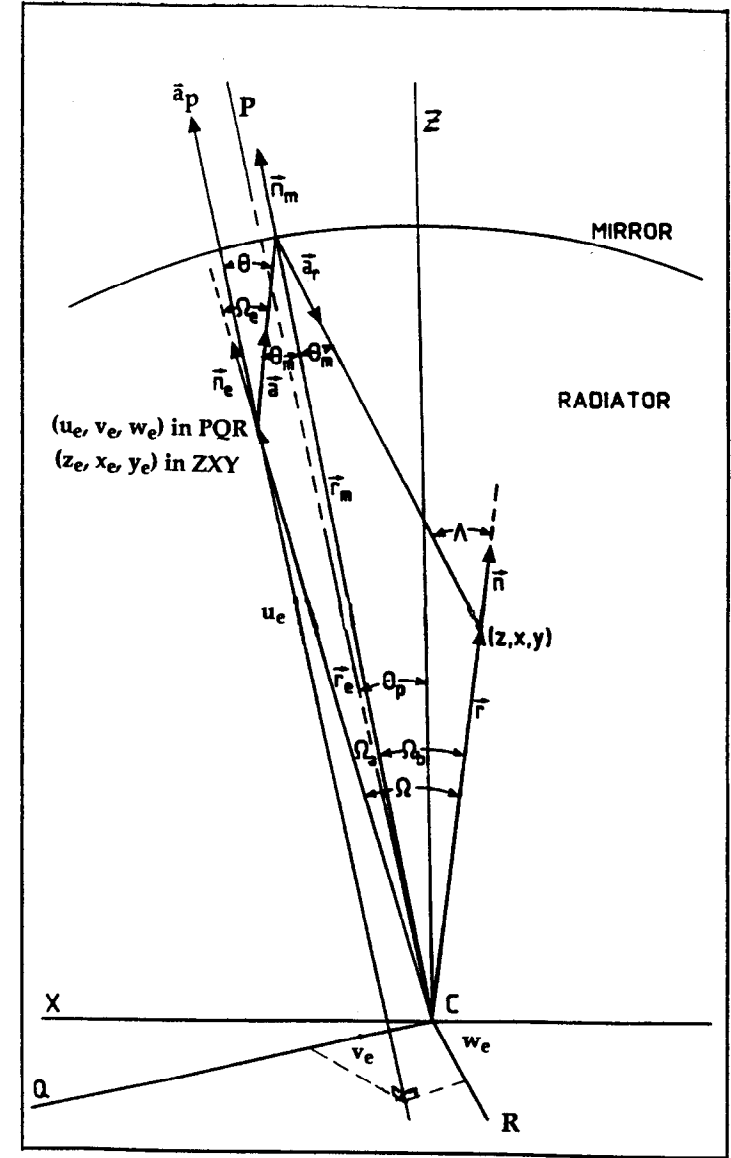


Fig. A1. The geometry of a mirror-focused ring image defined by the mirror center of curvature C, the Z axis along the neutrino beam, the X axis horizontal, and the Y axis vertical. The PQR axes, centered on C, are defined so that P is parallel to the particle direction \bar{a}_p and Q and R are normal to \bar{a}_p (i.e., parallel to \bar{b}_p, \bar{c}_p). The emission point coordinates in the PQR system are u_e along and v_e and w_e normal to the track.

Table A1

The coefficients K_i , L_i , M_i (versus ζ_i) which determine $\sin\theta(\partial\theta/\partial\zeta_i) = FK_i + GL_i + M_i$ [see Eqs. (A1) and (A2)] with $r_a = r_e \sin\Omega_e = r_m \sin\theta_m = r \sin\Lambda$, and $r_b = r_e \cos\Omega_e$. The primes in rows $\zeta_i = \theta_p$, or ϕ_p , indicate a partial derivative with respect to this variable. Quantities found in these rows (mirror tracker) are defined as $s_z = rz_e \sin\Omega - zr_b$, $s_x = rx_e \sin\Omega - xr_b$, $s_y = ry_e \sin\Omega - yr_b$.

Three relations are needed to allow calculation of the derivatives $\partial\theta/\partial\zeta_i$ for use in evaluation of the errors in Eq. (18); they are Eqs. (34), (35), and (39) (the first). Given these relations, it is straightforward to obtain the relation $\frac{\partial\theta}{\partial\zeta_i} = \frac{FK_i + GL_i + M_i}{\sin\theta}$ where

$$K_i = \frac{r_a}{\sqrt{r^2 - r_a^2}} \left(\frac{\partial \ln r}{\partial \zeta_i} \right) - Jr_a \left(\frac{\partial \ln r_e}{\partial \zeta_i} \right);$$

$$J = \frac{1}{\sqrt{r^2 - r_a^2}} - \frac{2}{\sqrt{r_m^2 - r_a^2}};$$

$$L_i = \frac{1}{\tan\Omega} \left[\frac{\partial \ln(rr_e)}{\partial \zeta_i} \right] - \frac{1}{r_e \sin\Omega} \frac{\partial}{\partial \zeta_i} (zz_e + xx_e + yy_e); \quad (A1)$$

$$M_i = \frac{\sin\Omega'}{\sin\Omega} \frac{\partial}{\partial \zeta_i} \left(\frac{u_e}{r_e} \right) - \frac{\sin\Omega_e}{\sin\Omega} \frac{\partial}{\partial \zeta_i} \left(\frac{u}{r} \right);$$

with

$$F = \frac{ru_e \cos\Omega' - ru_e \cos\Omega_e}{r_e \sin\Omega(1 + Jn_b)},$$

$$G = F + \frac{\sin\Omega_e}{\sin^2\Omega} \left[\frac{u \cos\Omega}{r} - \frac{u_e}{r_e} \right]; \quad (A2)$$

these are explicitly evaluated in Table A1 for both mirror and normal trackers.

ζ_i	K_i	L_i	M_i
z	$\frac{zr_a}{r^3 \cos\Lambda}$	$\frac{zr_b - rz_e}{r^2 r_e \sin\Omega}$	$\left(\frac{uz}{r^2} - apz \right) \frac{\sin\Omega_e}{r \sin\Omega}$
x	$\frac{xr_a}{r^3 \cos\Lambda}$	$\frac{xr_b - rx_e}{r^2 r_e \sin\Omega}$	$\left(\frac{ux}{r^2} - apx \right) \frac{\sin\Omega_e}{r \sin\Omega}$
y	$\frac{yr_a}{r^3 \cos\Lambda}$	$\frac{yr_b - ry_e}{r^2 r_e \sin\Omega}$	$\left(\frac{uy}{r^2} - apy \right) \frac{\sin\Omega_e}{r \sin\Omega}$
Mirror tracker			
z_e	$-\frac{Jz_e \sin\Omega_e}{r_e}$	$\frac{rz_e \cos\Omega - zr_e}{r_e^2 \sin\Omega}$	$\left(apy - \frac{z_e u_e}{r_e^2} \right) \frac{\sin\Omega'}{r_e}$
x_e	$-\frac{Jx_e \sin\Omega_e}{r_e}$	$\frac{rx_e \cos\Omega - xr_e}{r_e^2 \sin\Omega}$	$\left(apy - \frac{x_e u_e}{r_e^2} \right) \frac{\sin\Omega'}{r_e}$
y_e	$-\frac{Jy_e \sin\Omega_e}{r_e}$	$\frac{ry_e \cos\Omega - yr_e}{r_e^2 \sin\Omega}$	$\left(apy - \frac{y_e u_e}{r_e^2} \right) \frac{\sin\Omega'}{r_e}$
θ_p	0	0	$\frac{s_z a_{pz}' + s_x a_{px}' + s_y a_{py}'}{r_e \sin\Omega}$
ϕ_p	0	0	$\frac{s_z a_{pz}' + s_x a_{px}' + s_y a_{py}'}{r_e \sin\Omega}$
Normal tracker			
u_e	$-\frac{Ju_e \sin\Omega_e}{r_e}$	$\frac{ru_e \cos\Omega - (\bar{r} \cdot \bar{a}_p) r_e}{r_e^2 \sin\Omega}$	$\frac{(r_e^2 - u_e^2) \sin\Omega'}{r_e^3 \sin\Omega}$
v_e	$-\frac{Jv_e \sin\Omega_e}{r_e}$	$\frac{rv_e \cos\Omega - (\bar{r} \cdot \bar{b}_p) r_e}{r_e^2 \sin\Omega}$	$\frac{u_e v_e \sin\Omega'}{r_e^3 \sin\Omega}$
w_e	$-\frac{Jw_e \sin\Omega_e}{r_e}$	$\frac{rw_e \cos\Omega - (\bar{r} \cdot \bar{c}_p) r_e}{r_e^2 \sin\Omega}$	$\frac{u_e w_e \sin\Omega'}{r_e^3 \sin\Omega}$
θ_p	0	$\frac{zz_e' + xx_e' + yy_e'}{-r_e \sin\Omega}$	$\frac{za_{pz}' + xa_{px}' + ya_{py}'}{-r \sin\Omega / \sin\Omega_e}$
ϕ_p	0	$\frac{zz_e' + xx_e' + yy_e'}{-r_e \sin\Omega}$	$\frac{za_{pz}' + xa_{px}' + ya_{py}'}{-r \sin\Omega / \sin\Omega_e}$